2018-01-01

Computational Modeling Of Ring DNA-Carbon Nanotube Sensors

Aliasghar Alizadehmojarad
University of Texas at El Paso, ali.alizadehmojarad@gmail.com

COMPUTATIONAL MODELING OF RING DNA-CARBON NANOTUBE SENSORS

ALIASGHAR ALIZADEHMOJARAD

Master's Program in Chemistry

APPROVED:

Lela Vukovic, Ph.D., Chair

Ricardo Bernal, Ph.D.

Tunna Baruah, Ph.D.

Charles Ambler, Ph.D.
Dean of the Graduate School

Dedication

To science, as an infinitesimal contribution

COMPUTATIONAL MODELING OF RING DNA-CARBON NANOTUBE SENSORS

by

ALIASGHAR ALIZADEHMOJARAD, M.Sc.

THESIS

Presented to the Faculty of the Graduate School of

The University of Texas at El Paso

in Partial Fulfillment

of the Requirements

for the Degree of

MASTER OF SCIENCE

Department of Chemistry

THE UNIVERSITY OF TEXAS AT EL PASO

August 2018

Acknowledgements

I would like to thank my adviser, Dr. Lela Vuković, for thoroughly guiding and supporting me to take the steps throughout my thesis. I would also acknowledge Dr. Markita Landry and her group member, Abraham G. Beyene at the University of California Berkeley, providing us with experimental data. I appreciate Dr. Petr Král at the University of Illinois at Chicago for his useful discussions. I acknowledge Texas Advanced Computing Center (TACC) for providing us with the computational power. I acknowledge the Department of Chemistry at the University of Texas at El Paso for supporting our research under startup funding. I appreciate my former colleague, Dr. Suresh Gorle, for helpful discussions.

Abstract

Non-covalent interactions between single-stranded DNA (ssDNA) oligonucleotides and carbon nanotubes have provided a unique class of tunable chemistries for applications in nanotube chirality purification, gene delivery, electrochemistry, and nanosensor development. However, mechanistic insight into both the photophysical and intermolecular phenomena underlying their utility in such applications is lacking, resulting in non-systematic approaches to producing DNA-nanotube based technologies. In this work, we explore the molecular interactions between ssDNA polymers, in particular $(GT)_6$, and single-walled carbon nanotubes (SWNT) in an ultrasensitive nanosensor for a modulatory neurotransmitters dopamine. Classical molecular dynamics simulations show that $(GT)_6$ oligonucleotides adopt ordered, ring-like conformations around SWNT in contrast to the helical adsorption pattern observed for most previously used longer SWNT-adsorbed ssDNA sequences. We also performed replica exchange molecular dynamics simulations to produce a free energy landscape of $(GT)_6$ conformations at SWNT, and determined that the ring-like structure of $(GT)_6$ at SWNT is one of the most stable conformations, i.e. a free energy minimum structure. Our results show that the ring-like and helical conformations of ssDNA also leave two distinct electrostatic potential footprints at the SWNT surface. We show that adsorbed dopamine has a synergistic effect on ssDNA-SWNT hybrid materials. It leads to disruption of ssDNA conformation and their electrostatic footprint at SWNT surface, explaining more intense optical response of SWNT upon adsorption of dopamine.

Table of Contents

Introduction

At the crux of biomolecule sensing lies molecular recognition, which is central to therapeutics, diagnostics, biological signaling, pre-clinical models, and sensor platforms. *Ab initio* design of synthetic molecular recognition elements, and transducing the signal representing the recognition event, constitute the two primary challenges in biosensor design. Natural evolution of molecular recognition has yielded antibody-antigen complexes that have exquisite selectivity and binding affinities. However, their isolation and incorporation into sensing devices is limited by their instability outside of narrow physiological conditions. Furthermore, most biomolecules of interest lack molecular recognition elements. Therefore, a big limitation of biomarker detection has been the detection of biomolecules that have no naturally occurring molecular detection counterpart that we can borrow from nature. To this end, there is a great opportunity to combine optically active nanomaterials with polymers to rationally design synthetic nanosensors for biomolecule detection, particularly for small signaling molecules. In particular, drugs that mimic, block, or alter the concentration of the three primary neurotransmitters (dopamine, norepinephrine, serotonin) make the core arsenal of treatment for many neurological and psychiatric disorders. Furthermore, most drugs of abuse target cellular processes that directly interfere with the dynamics of modulatory neurotransmitters in the brain, making dopamine in particular central to our understanding of the biology of addiction. However, current methods used to diagnose disease and validate drug efficacy rely largely on questionnaires and behavioral observations. Therefore, the development of optical sensors that can record the fast dynamics of modulatory neurotransmitters stands to impact our ability diagnose disease, test drug efficacy and enhance our understanding of the biology of neuromodulation.

In the present thesis, we present a new approach to nanosensor development that utilizes joint computational modeling (the basis of this thesis) and experimental work of our collaborators, the group of Prof. Markita Landry. The nanosensors explored in modeling and experiments combined nanotube exciton engineering with synthetic bio-mimetic polymers. The experiments of

Prof. Landry group demonstrate that exciton recombination *and* analyte selectivity can be controlled with polymers adsorbed to the surface of semiconducting single-wall carbon nanotubes, producing two reversible neurotransmitter sensors: one for dopamine, and one for norepinephrine, each with $\Delta F/F_0$ (F_0 and ΔF respectively represent baseline fluoresce and changes in intensity of fluoresce response of nano-sensor after addition of 100 μM of dopamine) fluorescence signals exceeding 2500% and 3500%, respectively. We hypothesized that the electrostatic potential at the SWNT surface influences the exciton relaxation pathway in very important ways. Strong local electrostatic potential on SWNT surface is mediated by the polarity of the SWNT environment (for example, polymer wrapping) that in turn impacts radiative recombination rates and sets the baseline intensity of photoluminescence. By controlling the wrapping around the carbon nanotube, it should be possible to optimize a molecular sensor's response to the presence of an analyte.

SWNTs are rolled cylindrical sheets of graphene that exhibit remarkable mechanical, electrical and optical properties. As a result, they have found relevance in numerous fields, such as electronics, materials research, and biological imaging and therapeutics [1-4]. Their versatile properties are evidenced by the myriad of uses they have found in nanotechnology, design of high performance composite materials and molecular sensing applications, to name a few [5-7]. In particular, within the context of biological research, the field of optical imaging is well positioned to benefit from carbon nanotube's exceptional photostability and fluorescence in the near infrared, which coincides with a local minima in scattering and absorption spectra of water and tissue, enabling deep tissue imaging at a high spatial resolution. Besides serving as contrast agents for imaging, polymer functionalized carbon nanotubes have been used to design highly sensitive molecular recognition moieties [8, 9]. Molecular sensing uses polymer-functionalized nanotubes consisting of nanoparticle-polymer corona whose fluorescence can be modulated in a unique way by a chemical analyte. The modulation in fluorescence arises from an increase or decrease in quantum efficiency, or from a shift in the optical band gap of the nanoparticle. Molecular recognition that takes advantage of the fluorescence modulation of the SWNT-polymer corona is known as corona phase molecular recognition (CoPhMoRe).

While a wide range of molecular sensors that use CoPhMoRe have been reported [5, 9-12], in this thesis, I will describe nucleic acid wrapped carbon nanotubes that have been shown to detect modulatory neurotransmitters. In particular, the nucleic acid polymers explored in this thesis include single stranded G and T DNA nucleotide repeats, $(GT)_{15}$ and $(GT)_6$. $(GT)_{15}$ wrapped SWNTs have shown selective molecular recognition for dopamine, a key neurotransmitter implicated in a wide range of critical brain functions, such as learning, motor skills, and habit formation. Aberrations in dopamine brain chemistry are associated with numerous neurological and psychiatric disorders, such as Parkinson's disease, schizophrenia and addiction [13]. Furthermore, drugs of abuse almost exclusively act on receptors of these modulatory signaling molecules. As a result, nanosensors have significant implications for neuroscience, where a dearth of tools to probe nanoscale neurological processes has impeded a comprehensive understanding of how the brain both functions and malfunctions [14]. Nanotechnologies such as SWNT-based neurotransmitter sensors are an attractive tool for measuring brain chemistry, where their few-nm diameters can be non-invasively inserted into the extracellular space of brain tissue, and can report on neurochemical activity close to synaptic cleft where neurotransmission occurs. Furthermore, the fluorescence turn-on signal of SWNT based dopamine sensor is instantaneous and reversible, enabling imaging of fast dopamine dynamics with high temporal resolution, and without quenching or blinking. Consequently, SWNT based sensors are uniquely suited to probe processes at the spatial and temporal scales that match neural processes.

Selective polymer-mediated adsorption of the dopamine analyte on the SWNT sensor is thought to cause a fluorescence modulation that becomes the sensor signal [5, 11]. However, a molecular-scale understanding of the analyte-sensor recognition process is lacking, limiting our ability to (i) develop sensors with larger fluorescence signals needed for *in vivo* use, and (ii) develop sensors for key modulatory neurotransmitters, such as norepinephrine. Herein, we elucidate the dopamine-sensor molecular recognition process by mapping the electronic potential map on the nanosensor surface, and combine our knowledge of polymer adsorption and

electrostatic potential mediated exciton confinement to develop a norepinephrine sensor with a 3500% fluorescent turn-on response.

List of Figures

1 Methods

Throughout my thesis, I have used classical molecular dynamics (MD) simulation method. In this chapter, I first explain the classical mechanics equation governing the systems, which we studied through the method. I then describe the interaction parameters defining interactions among atomic species in the systems of interest. I also discuss the integration method to solve the equations of motion under the thermodynamic ensemble of interest. Additionally, I discuss free energy concept and its implementation using MD simulation.

1.1 Classical molecular dynamics

Throughout my thesis, I have used atomistic classical MD simulations method. The method includes solving classical equation of motion using Newton's equations of motion. Solving Newton equation of motion of a system including N particles provides us with time-evolution of positions and momenta of particles. Newton's equations of motion for an atomic system of N particles are defined as follows:

$$m_i \frac{\partial^2 \vec{r_i}}{\partial t^2} = \vec{f_i} \qquad \vec{f_i} = -\frac{\partial}{\partial \vec{r_i}} U(\vec{r_1}, \vec{r_2}, \dots \vec{r_N}) \tag{2.1}$$

For solving the equation Eq. 2.1, we need to calculate forces $\vec{f_i}$ exerted on atom i by all the other atoms present in the system. To calculate these forces, we need to determine the atomic mass (m_i) and potential energy U, which is function of 3N atomic coordinates ($\vec{r_1}, \vec{r_2}, \dots \vec{r_N}$). According to eq. 2.1, obtaining potential forms ($U(\vec{r_1}, \vec{r_2}, \dots \vec{r_N})$) and solving the above equation numerically and efficiently are two crucial factors, which have been considered in all MD engines, such as NAMD [15]. Potential forms are defined through force fields approximating interaction parameters of atoms.

1.2 Force field

Force fields are composed of functions and interaction parameters of atoms defining the potential energy of an atomic system. The parameterization of force fields, such as CHARMM [16], mainly used in this thesis, are performed by means of quantum mechanical calculations. The

calibration and verification of force field parameters need to be verified and calibrated by comparing experimental and simulated thermodynamics properties including heats of vaporization and solvation free energy, etc. [17, 18].

Force field parameters are divided into two groups, including bonded (defining intramolecular interactions) and non-bonded (defining intermolecular interactions) ones. Bonded and non-bonded interaction parameters determine the potential energy of a system, $V_N = U(\overrightarrow{r_1}, \overrightarrow{r_2}, \ldots \overrightarrow{r_N})$ through sum of bonded and non-bonded interaction energies:

$$V_N = \sum V_{N,bonded} + \sum V_{N,non-bonded} \tag{2.2}$$

Bonded potentials ($V_{N,bonded}$) describe intramolecular interactions including stretching, bending and torsions depicted in Figure 1. $V_{N,bonded}$ of CHARMM force field [14] is composed of bond, angle, dihedral and improper dihedral potentials, which are explained as follows:

$$V_{bond} = \sum_{bond\ i} k_i^{bond}(r_i - r_{0i})^2 \tag{2.3}$$

$$V_{angle} = \sum_{angle\ i} k_i^{angle}(\theta_i - \theta_{0i})^2 \tag{2.4}$$

$$V_{dihedral} = \sum_{dihedral\ i} k_i^{dihedral}\,[1 + \cos(n_i\emptyset_i - \gamma_i)], \qquad n_i \neq 0 \tag{2.5}$$

$$V_{improper} = \sum_{improper\ i} k_i^{improper}(\emptyset_i - \gamma_i)^2, \qquad n_i = 0 \tag{2.6}$$

Above, V_{bond}, V_{angle} and $V_{improper}$ are described using the harmonic potential forms, which may be computed by using the defined (k_i^{bond}, k_i^{angle}, $k_i^{improper}$) and associated instantaneous internal coordinates (r_i), angles (θ_i), dihedrals and improper dihedrals ($\emptyset_i$), which can differ from their equilibrium values (r_{0i}, θ_{0i}, γ_i). The equilibrium values r, theta, and gamma, provide states of minimum stretching, bending and torsional energies. Cosine function is used to define $V_{dihedral}$, which is determined by introducing force constant $k_i^{dihedral}$, periodicity n_i and dihedrals ($\emptyset_i$) varying from γ_i.

Non-bonded potential energies include Coulomb and van der Waals (vdW) potentials, which are pair-wise interactions. The below formulation is defined to determine the long-range Coulomb energies between atoms i and j, which carry q_i and q_j charges, respectively:

$$V_{Coul}(r_{ij}) = \sum_i \sum_{j>i} \frac{q_i q_j}{4\pi\epsilon_0 r_{ij}} \tag{2.7}$$

Above, ϵ_0 and r_{ij} denote vacuum permittivity and distance between the center of atoms. The short-range Lennard-Jones potential is used to describe van der Waals (vdW) interactions

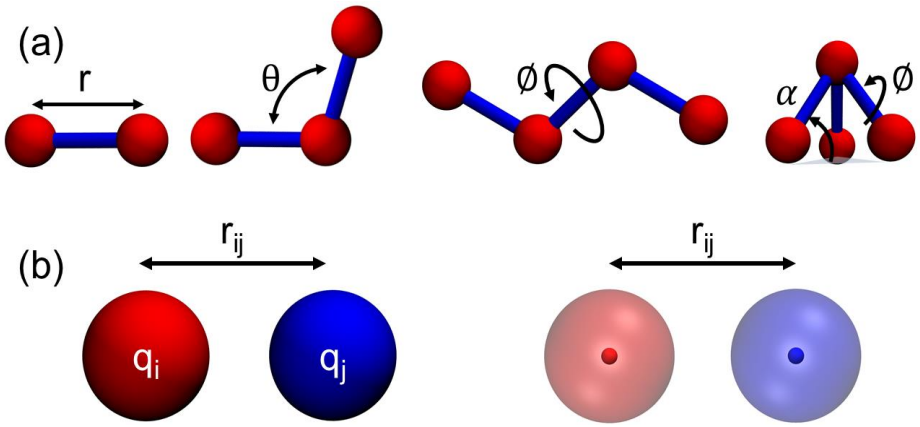

Figure 1 Bonded and non-bonded interaction parameters. (a) bonded interaction parameters: r denotes bond stretching, θ shows the bond angle, $\emptyset$ represents the dihedral angle, small out-of-plane angle α (which is not used in improper dihedral potential model) can be satisfied by improper dihedral angle $\emptyset$. (b) the distance between two non-bonded particles carrying partial charges q, is r_{ij}.

between atom pair i-j. The Lennard-Jones potential is composed of two terms including repulsion and dispersion:

$$V_{LJ}(r_{ij}) = \sum_{i} \sum_{j>i} \varepsilon_{ij} \left[\left(\frac{R_{min,ij}}{r_{ij}} \right)^{12} - 2 \left(\frac{R_{min,ij}}{r_{ij}} \right)^{6} \right] \tag{2.8}$$

where r_{ij} is the distance between atoms i and j, and $R_{min,ij}$ and ε_{ij} are determined from the Lorentz-Berthelot:

$$R_{min,ij} = \frac{R_{min,i} + R_{min,j}}{2}, \varepsilon_{ij} = \sqrt{\varepsilon_i \varepsilon_j} \tag{2.9}$$

where $R_{min,i}$, $R_{min,j}$ and ε_i, ε_j represent the radii and potential well depths of particles i and j, respectively. Throughout the thesis, I have used CHARMM force field, which is one of the mostly used to simulate biological systems.

1.3 Integration method for MD

Throughout MD simulations, time evolution of positions and velocities of atoms may be obtained by taking the integral of Newton's equations of motion. NAMD [15] was used to perform MD simulations throughout the thesis. NAMD hires the velocity-Verlet integration algorithm, which takes given atom's position (R_n), velocity (v_n) and force (f_n) at each time step (n) and outputs these values for the next step (R_n, v_n, f_n) by applying finite difference concept. The velocity-Verlet algorithm is performed according to the following steps:

$$\begin{aligned}
&\text{“half-kick”} && v_{n+1/2} = v_n + m^{-1} f_n \cdot \Delta t/2, \\
&\text{“drift”} && R_{n+1} = R_n + v_{n+1/2} \cdot \Delta t, \\
&\text{“compute force”} && f_{n+1} = f(R_{n+1}), \\
&\text{“half-kick”} && v_{n+1} = v_{n+1/2} + m^{-1} f_{n+1} \cdot \Delta t/2.
\end{aligned} \tag{2.10}$$

The advantages of the velocity-Verlet algorithm include evaluation of only one force at every step, time reversibility and symplecticity of the algorithm leading to conserved momentum.

1.4 Periodic boundary conditions (PBC)

Molecular simulation methods, such as atomistic MD simulations have limitations to simulate macroscale systems containing a large number of atoms (Avogadro's number). MD simulation packages can currently run simulations including a much smaller number of atoms (10^7) than Avogadro's number ($\approx 6.022 \times 10^{23}$). To resolve the size issue, periodic boundary conditions (PBC) are defined in simulations in three dimensions or two dimensions (slab boundary condition). Through PBC, the original simulation unit cell interacts with its adjacent periodic images in each direction. Therefore, the vacuum boundaries of the system causing artifacts can be avoided.

1.5 Ensembles

According to the condition of the experiments, different thermodynamics ensembles can be applied to implement MD simulations. There are several simulation ensembles, such as NVE (the number of particles (N), volume (V) and total energy (E) of the system are held constant), NVT (N, V and temperature (T) are held constant), and NPT (N, V, and pressure (P) are held constant). NPT ensemble was mainly used in this thesis. The coupling of pressure and temperature of the systems was performed through using Langevin technique. This technique damps the T and P fluctuations by adding a damping and fluctuating terms to the Newton's equation of motion:

$$\mathrm{m}\frac{\partial^2 \vec{\mathrm{r}}}{\partial \mathrm{t}^2} = \mathrm{m}\dot{\mathrm{v}} = \mathrm{F}(\mathrm{r}) - \gamma_{\mathrm{Lang}}\mathrm{mv} + \sqrt{2\gamma_{\mathrm{Lang}}\mathrm{k_B Tm}}\,\mathrm{G}(\mathrm{t}) \tag{2.11}$$

where r, t, m, v and F respectively denote coordinate, time, mass, velocity and force, which is the gradient of the potential based on the Newton's equations of motion. γ_{Lang}, $\mathrm{k_B}$ and T denote friction factor (depending on the systems and defined by user), Boltzmann constant and temperature. $\mathrm{G}(\mathrm{t})$ denotes a univariate Gaussian process.

The second and third terms in Eq. 2.11 are damping and fluctuating terms, respectively. γ_{Lang} is responsible for controlling the magnitudes of damping and fluctuating terms. If $\gamma_{\mathrm{Lang}} \rightarrow 0$, the Eq. 2.11, which is called the Langevin equation dynamics, becomes identical to the Newton's

equations of motion. In fact, introduction of γ_{Lang} simulates an existing reservoir at a user-defined temperature T, which is coupled to the system to damp the fluctuations.

1.6 Simulation parameters

Throughout the thesis, all atoms of a typical system interact through non-bonded interaction energies including both Coulombic (long range) and vdW (short range) potentials. The cut-off distance for vdW potential energies are explicitly defined to ignore the interaction energies beyond the cut-off distance. In CHARMM force field, both vdW cut-off distance is usually set to 1.2 nm. Smoothing this potential beyond the cut-off distance is necessary to avoid potential artifacts due to sharp truncation of vdW potentials. The smoothness occurs between the cut-off distance and the switching distance (usually 0.8 nm), which is defined by end user. Coulomb potential is evaluated for atoms whose distances are beyond the vdW cut-off distance. Particle-mesh Ewald (PME) method [19] is applied to efficiently calculate the Coulombic electrostatic interactions in periodic systems [15]. Throughout this thesis, we used explicit solvent (water) molecules, which were modeled by the TIP3P water model. Additionally, the time step for integration is usually set to 2 fs.

1.7 Free energy calculations using classical MD simulations

The classical particles are space-localized particles, in contrast to space-delocalized quantum particles. If the 3 spatial and 3 momentum coordinates of a classical particle are known, the state of the particle is known. Correspondingly, the state of system including N classical particles can be determined by having 6N spatial and momentum coordinates. This state is a representative vector in the phase space of all other possible states of the system. To describe the global phase space of a many-particle system, measurable thermodynamics state variables of each state, such as temperature, pressure, density, free energy, entropy, etc. must be determined. In fact, the Gibbs free energy of the system , which is composed of N particles at temperature T and pressure P, defines the state of the system in the global phase space. In the other words, the probability of observing a molecular system (many-particle system) in one state or another state

can be explained by the free energy differences between those two states. Based on thermodynamics, the maximum amount of obtainable work from a system subject to external constraints, such as N, P and T is determined by Gibbs free energy. The external constraints define the spontaneous evolution of the system along the Gibbs free energy.

The classical MD simulation is one of molecular simulations methods, which can be applied to calculate free energy differences between states of a system. MD simulation methods generate particles' trajectories comprising a data points, which are a part of the global phase space. Therefore, MD simulation trajectories can be an informative source to extract coordinates and velocities of the particles in the course of simulation. The mean force acting on every particle of the system can be computed along reaction coordinates. One-dimensional representative path of a process, such as conformational transition, solvation of a molecule, binding of two molecules and so on, is called a reaction coordinate. Several methods have been developed to calculate free energy differences from MD simulations, such as umbrella-sampling [20], adaptive biasing force [21], thermodynamic integration [22], free energy perturbation [23], replica exchange MD (REMD) [24]. I took advantage of the REMD method in this thesis, as described in the next section.

1.8 Replica exchange molecular dynamics (REMD)

Molecular simulation methods generally need ergodic sampling of energy landscapes including many minima. Crossing the barriers between minima at ambient temperature during the possible simulation time scales is difficult. Therefore, the initial condition of the system largely can potentially affect the results. In regular MD simulations, the initial condition determines the explored region of the phase space by the simulated system. REMD simulation is one of the enhanced sampling methods enabling MD simulations to explore the much larger regions of phase space. Through implementing REMD simulations, the effect of initial condition on MD simulation results may potential vanish.

REMD methods are based on replica-exchange method (REM), originated in Monte Carlo algorithm. REM was initially adapted to MD simulations to study protein-folding. The REM

method is based on running several replicas at different temperatures in parallel. In REMD, several replicas of the same system are simulated by classical MD simulations at different temperatures. After some time passes (exchange time, τ_{exch}), the algorithm examines the energies of all the replica systems, and attempts an exchange, after which the replica simulated at T_i will continue to be simulated at T_j, and vice versa [23]. The exchange is performed according to the Metropolis criterion:

$$\mathrm{p(exchange)} = \begin{cases} \exp(\Delta); & \Delta < 0 \\ 1; & \Delta \geq 0 \end{cases} \tag{2.12}$$

where p is the acceptance probability, Δ is $\left(E_i - E_j\right)\left(\frac{1}{kT_i} - \frac{1}{kT_i}\right)$. E, k and T represent potential energy, Boltzmann constant and temperature. i and j subscripts denote replicas i and j.

If a simulation with higher temperature has lower energy than the simulation with lower temperature or vice-versa, the temperature exchange is successful and it occurs automatically. After temperature exchange between neighboring replicas is attempted, simulation of all replicas resume running until the next exchange occurs. It leads to having unsorted replicas at the end of REMD simulations. For this reason, sorting replicas based on their starting temperature must be performed. **Figure 2** schematically shows the parallel REMD algorithm. The exchange frequency of the REMD algorithm, which affects the acceptance and rejection of exchange attempts, is defined by the user.

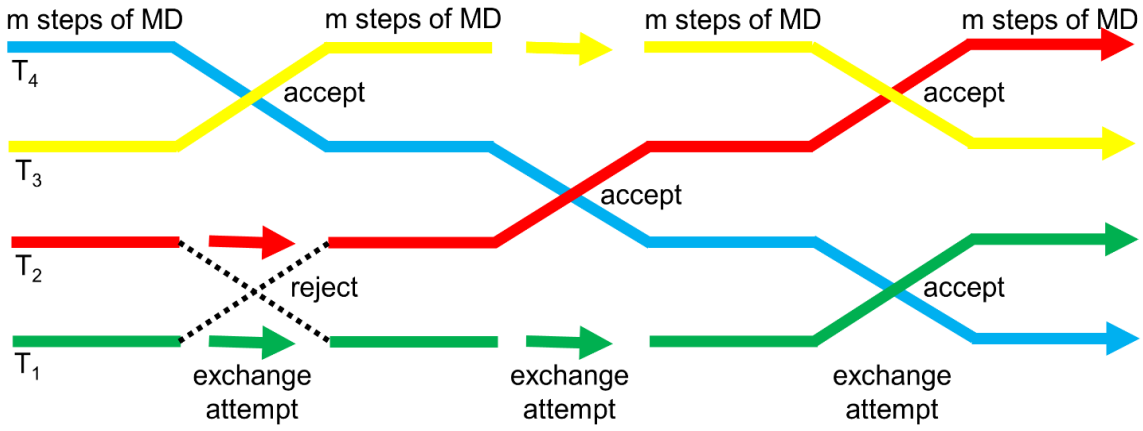

Figure 2 Running REMD algorithm in parallel. T_4 and T_1 represent highest and lowest temperatures, respectively

Sorted replicas include well-sampled trajectories of the system, which explored a larger areas in phase space at a given fixed temperature, which may contain multiple free energy minima. Instead of showing the free energy of simulated systems as a function of 3N coordinates, it is usually more useful to show the free energy as a function of reduced coordinates, which we call reaction coordinates, and which clearly define states of interest for the studied system. Choosing a proper reaction coordinates enables us to create an appropriate and rugged free energy landscape showing the free energy minima. The obtained free energy landscape leads to calculating free energy barriers between the most stable and probable states and less probable ones. For example, in the context of discovering protein folding pathways, a free energy landscape provides a very useful information regarding the most probable protein folding pathway. Free energy along the reaction coordinates are calculated by the relationship between the free energy G, and two dimensional probability distribution of data points of reaction coordinates.

$$\Delta G(x,y) = -k_B T \ln(Z) \qquad Z = \frac{P(x,y)}{P_{max}(x,y)} \tag{2.13}$$

By the definition, the free energy (ΔF) is a state function of reaction coordinates and Z is partition function. x, y denotes the data points of reaction coordinates 1 and 2, respectively. Reaction coordinates could be any order parameters measuring reaction progress clearly, such as root mean square displacement (RMSD), dihedral angle, bond distance, etc. Z partition function can be simplified as a measure on the probability space, $P(x,y)/P_{max}(x,y)$. $P(x,y)$ is two dimensional probability along reaction coordinates x, y.

2 Computational modeling of ring DNA-carbon nanotube sensors

2.1 Introduction

SWNTs have distinctive electronic, photophysical, and molecular transport properties that have made them attractive for a diverse field of applications in sensing [5], electronics [6], and nanofluidics [25]. SWNT fluorescence originates in a recombination of excitons, which are confined in one dimension (1D). Despite the fact that this SWNT fluorescence exhibits a high degree of photostability, it is sensitive to the nanotube geometric and electronic structures (diameter and chiral angle), including a local chemical environment [25]. This SWNT local chemistry sensitivity has been leveraged for the synthesis of optical nanosensors. In such systems, polymer functionalization serves a dual purpose of forming stable SWNT colloidal suspensions, while simultaneously conferring the SWNT a selective molecular recognition capability [5]. Several SWNT based optical nanosensors with selective analyte mediated modulations in fluorescence quantum yield or shifts in fluorescence peaks have been reported [4, 5, 8-12].

Synthesizing suitable elements capable of transducing *in vivo* signals, representing molecular recognition events, constitutes the primary challenge in the design of nanosensors. The versatility and ease with which different types of SWNTs can be functionalized by polymers provides a great opportunity for a rational design of synthetic nanosensors capable of detecting biomolecules. Despite several reports of SWNT-based nanosensors, a robust pathway to translate SWNT nanosensors for *in vivo* applications remains elusive. We attribute these two limitations – a rational design and an *in vivo* implementation – to a lack of fundamental understanding in how hybrid nanomaterials of SWNT with surface-adsorbed polymers enable their selective fluorescence modulation by molecular analytes. This knowledge gap is evident during nanosensor discovery, which relies on tedious low-throughput screening, while it remains unclear how the nanosensor performance can be tuned once a discovery has been made.

Nanosensor characterization techniques are lacking in two important aspects. First, analyte concentrations encountered under physiological conditions may not overlap with reported nanosensor dynamic range. Second, fast video-rate fluorescence imaging, required for capturing

transients in analyte concentration *in vivo*, require strong turn-on nanosensors to maintain high signal-to-noise during imaging. As such, successful demonstration of nanosensors *in vitro* that do not account for strength of turn-on response, nanosensor signal-to-noise ratio, and physiologically-relevant dynamic range, will struggle to find application *in vivo*.

In this work, we report a high turn-on nanosensor for dopamine. Experiments performed by the Landry group demonstrated that a sequence-specific 'short' single strand DNA (ssDNA) polymers-covered SWNT nanosensor is one of the optimized nanosensors for sensing dopamine and norepinephrine. We demonstrate that we can tune SWNT exciton recombination with ssDNA adsorbed to the surface of SWNT. Polymer adsorption impacts the radiative and non-radiative exciton recombination rates, and sets the baseline intensity of SWNT photoluminescence. Sequence specific 'short' single strand DNA (ssDNA) polymers produce strongly quenched SWNT baseline fluorescence and a strong turn-on response to dopamine and norepinephrine, a desirable signal transduction mechanism for *in vivo* molecular sensing and imaging.

Through classical molecular dynamics (MD), we identify polymer-induced 'electrostatic footprinting' on the SWNT surface, which likely mediates exciton recombination pathways and thus influences analyte mediated fluorescence modulation. We propose how these insights can be leveraged for nanosensor discovery, or for tuning the performance of those nanosensors already developed.

2.2 Methods

2.2.1 Molecular dynamics simulations

Atomistic simulations were conducted to investigate single stranded DNA-SWNT conjugates with and without added dopamine neurotransmitter molecules. In all simulations, conjugates of (9,4) SWNT with $(GT)_{15}$ and $(GT)_6$ molecules were prepared. (9,4) SWNT segments, 66.73 Å in length, were built in VMD [26]. The initial configurations of $(GT)_{15}$ and $(GT)_6$ molecules were built in Material Studio [27] with nucleotides arranged to form helical conformations with radii several angstroms wider than the radius of the (9,4) SWNT. The helical

DNAs were positioned to wrap SWNTs, with DNA bases not pre-adsorbed on the SWNTs surfaces. The length of the SWNT was selected to result in the optimal SWNT surface coverage by the adsorbed $(GT)_{15}$ ssDNA via base stacking, which prevents excessive ssDNA diffusion on SWNT. The prepared DNA-SWNT conjugates were solvated with TIP3P water and neutralized with 0.1 M NaCl with *solvate* and *ionize* VMD plugins [26], respectively. In simulations of DNA-SWNT conjugates with dopamine, two dopamine molecules were placed ~10 Å away from SWNTs into pre-relaxed systems prepared without dopamine. The final systems contained approximately 11,000 atoms.

The systems were described with CHARMM36 and CHARMM general force field (dopamine) parameters [16, 28, 29]. MD simulations were performed with NAMD2.11 package [15]. All the simulations were conducted with Langevin dynamics (Langevin constant γ_{Lang} = 1.0 ps^{-1}) in the NPT ensemble, where temperature and pressure remained constant at 310 K and 1 bar, respectively. The particle-mesh Ewald (PME) method was used to calculate Coulomb interaction energies, with periodic boundary conditions applied in all directions [19]. The timestep was set to 2.0 fs. The evaluation of long range van der Waals and Coulombic interactions was performed every 1 and 2 time steps, respectively. After 1,000 steps of minimization, solvent molecules were equilibrated for 2 ns around the DNA and SWNTs, which were restrained using harmonic forces with a spring constant of 1 kcal/(mol $Å^2$). Then, the systems were equilibrated in 250 ns production MD runs, with restraints applied only on the edge SWNT atoms.

To analyze the electrostatic potential that the surroundings create at the SWNT surface, we computed potential energy maps at SWNT surfaces for several configurations of DNA-wrapped SWNTs. In each configuration, selected from equilibriation MD trajectories, SWNT and DNA atoms were restrained with a hard (1.0 kcal/mol/$Å^2$) and soft (0.1 kcal/mol/$Å^2$) harmonic restraint, respectively, and simulated for 1 ns. We evaluated the potential energy map at the SWNT surface by averaging electrostatic potential energy contributions and Lennard-Jones contributions from 1 ns simulations of restrained systems. Electrostatic potential energy of each SWNT atom was

computed by setting its charge to q = −1e for the purpose of evaluating the electrostatic potential energy (in performed 1 ns simulations, each atom had the charge q = 0). The average potential energy of each carbon atom in its environment was evaluated with the NAMDEnergy plugin in VMD [26] (each 1 ns trajectory resulted in 500 potential energy data points).

2.2.2 Interaction energy between electron and hole clouds mobile at SWNT surface

We believe that potential signature left on the SWNT surface by ssDNA affects the exciton annihilation pathway. Exciton is composed of an e-hole pair, which is mobile at the SWNT surface. The interaction between e and hole could be described based on the electrostatic potential, in the simplest approximation. For this reason, any polar and charged species can largely affect their interaction and exciton annihilation pathway. Therefore, calculating the interaction energies between e and hole clouds, which are mobile at the SWNT surface is useful for understanding how electrostatic signature left by ssDNA on the SWNT can modulate e-hole interactions.

Electron and hole clouds comprising created exciton through excitation, which is mobile at SWNT surface, interact according to Coulomb integral, as explained above. Due to electronic nature of SWNTs, they are categorized as quasi-1D materials. We assumed two-dimensional Coulomb potential (in cylindrical coordinates) to calculate interaction energy between charged surface segments 1 ($-dq_1$), which is located at (r_0, θ_1, z_1) and 2 (dq_2), which is located at (r_0, θ_2, z_2) (**Figure 3**). The same normalized Gaussian distributions were considered to describe the distributed positive, $\frac{1}{\sqrt{2\pi\sigma^2}} \cdot \exp\left(\frac{-(z_1-\mu_1)^2}{2\sigma^2}\right)$ and negative charges, $\frac{1}{\sqrt{2\pi\sigma^2}} \cdot \exp\left(\frac{-(z_2-\mu_2)^2}{2\sigma^2}\right)$ in electron and hole clouds. In view of statistics concept, μ and σ^2 represent respectively expected value and variance of the distributed data points in a normal Gaussian distribution. Accordingly, we derived the below formulation based on Coulomb integral [30] to compute analytically the total Coulomb energy between two stationary electron and hole clouds where the distance between their centers is $(\mu_2 - \mu_1)$ nm:

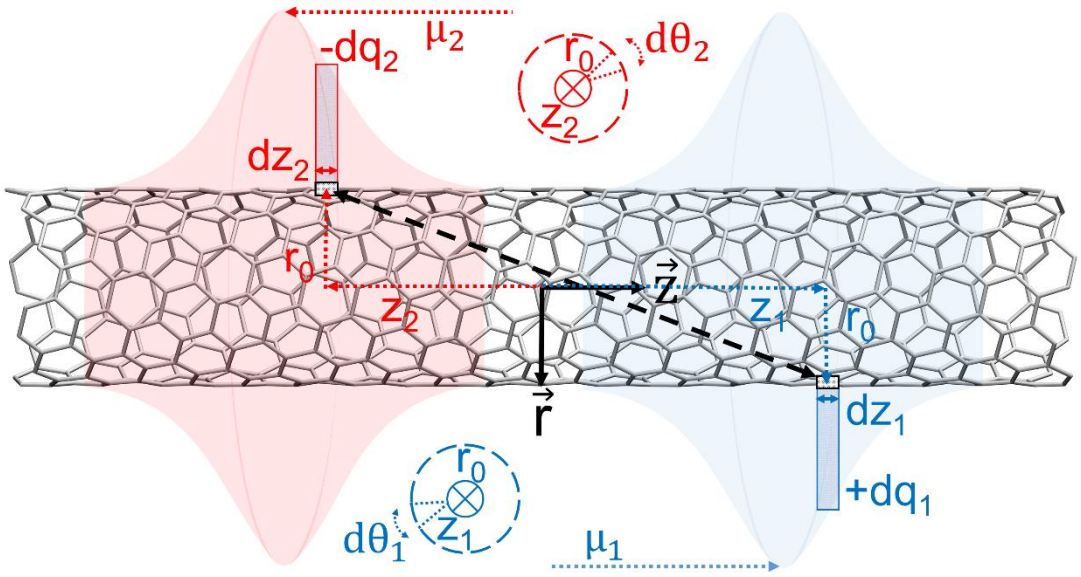

Figure 3 Schematic of cylindrical surface segments of Coulomb integral at the SWNT surface. The red and blue three dimensional distributed clouds surrounding the SWNT surface show the negative and positive clouds. $d\theta_2$, $dz_2$and $d\theta_1$, dz_1 represent the angular dimensions (radian), length dimensions (nm) of the surface segments carrying negative (dq_2) and positive (dq_1) partial charges, respectively. Red and blue dashed lines show the location of negatively and positively charged surface segments, respectively. Black dashed line shows the distance between surface segment 2 and surface segment 1 in cylindrical coordinates. μ_2 and μ_1 denotes the location of center of negative and positive clouds along z-axis. The origin of cylindrical coordinates was fixed in the middle of SWNT.

$$\frac{-e^2}{4\pi\varepsilon_0}\int_{-100}^{100}\int_{0}^{2\pi}\int_{-100}^{100}\int_{0}^{2\pi}\frac{{r_0}^2\cdot\left(\frac{1}{\sqrt{2\pi\sigma^2}}\right)^2\cdot\exp\left(\frac{-(z_2-\mu_2)^2}{2\sigma^2}\right)\cdot\exp\left(\frac{-(z_1-\mu_1)^2}{2\sigma^2}\right)}{\sqrt{2{r_0}^2-2{r_0}^2\cos(\theta_2-\theta_2)+(z_2-z_1)^2}}d\theta_1 dz_1 d\theta_2 dz_2$$

where, μ and σ determine the location of center of electron (or hole) cloud along z-axis and spread of charge on the cloud, respectively. ε_0 and r_0 denote the dielectric constant (which varies in hydrophobic or hydrophilic environment) and the radius of (9,4) SWNT, which is constant (0.4515 nm), respectively. We chose middle of SWNT along z-axis and center of SWNT circumference as the origin of coordinates. For the sake of clarity, surface segment is shown in **Figure 3**. The charge of this segment (dq) is determined based on its z coordinates and the cloud distribution function. The angular distance of the surface segment from the origin is described by dθ. The denominator of the integral shows the distance (shown in **Figure 3**) between two typical surface segments of electron and hole clouds. The charge on both positive and negative charged

clouds were distributed from -100 nm to +100 nm (which is also in the scale of real SWNT [**31**]) to make sure most part of charge of the clouds will be taken into account. To calculate the interaction energies between two mobile clouds with the same spread of charge on the cloud (σ=0.5 nm), the z coordinate of positive cloud was fixed at z_1=0, then the interaction energies were evaluated for different z_2 values varying from [-12 nm, 12 nm]. We repeat calculations for two other different σ values (1 nm and 2 nm). All the integrals were evaluated numerically by using MATLAB R2017a**.**

2.3 Results

2.3.1 SWNT circumference-length polymers yield large ΔF/F turn-on nanosensors for dopamine and norepinephrine

Dr. Landry research group designed fluorescent probes for neuromodulators dopamine (DA) and norepinephrine (NE) with requisite optical responses for *in vivo* implementation. Prior work has shown the fluorescence intensity of $(GT)_{15}$-SWNT increases by 60% ($\Delta F/F = 0.6$) upon exposure to 100 μM of DA (ref), which translates to $\Delta F/F = 0.3$ at peak physiological dopamine concentrations that follow burst neuronal firing events (~1-2 μM). (ref) Motivated by the goal of producing an *in vivo* compatible neuromodulator nanosensor for a broader dynamic range of physiological relevance, they synthesized a $(GT)_N$ based ssDNA polymer library for N = 4, 6, 7, 8, 12, 15, 19, 22, 26, and 30. Near infrared fluorescence and absorption spectroscopy were implemented to confirm that all sequences from N = 4 to N= 30 produced stable DNA-SWNT suspensions, as evidenced by sharply defined spectral line shapes corresponding to well known SWNT chiralities. They then measured each $(GT)_N$-SWNT nanosensor's response to 100 μM DA. DA addition increases SWNT fluorescence for all sequences (**Figure 4**). However, there exists a strong length-dependent trend in nanosensor response to dopamine, for which the previously reported $(GT)_{15}$-SWNT nanosensor represents an apparent minimum ($\Delta F/F_0 = 0.45$), and $(GT)_6$-SWNT a maximum ($\Delta F/F_0 = 24$) (**Figure 4a**). 'Short' $(GT)_N$ polymers ($N = 4, 6, 7, 8$) yield $\Delta F/F_0$ = 14, 24, 17, and 10 in response to 100 μM DA, respectively, for the (9,4) SWNT chirality.

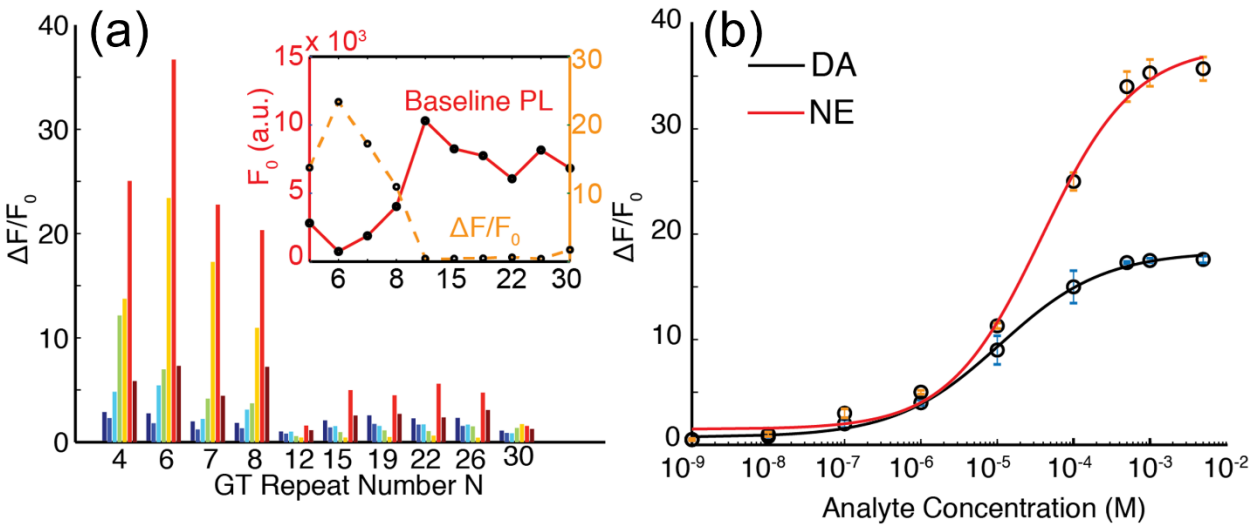

Figure 4 (provided by Abraham G. Beyene, Dr. Landry research group) Nanosensor response and selectivity for dopamine and norepinephrine as a function of polymer length. (a) $\Delta F/F_0$ of each sequence, for each SWNT chirality (8,3) dark blue, (6,5) blue, (7,5) cyan, (10,2) green, (9,4) and (7,6) yellow, (8,6) and (12,1) red, (10,3) and (10,5) maroon. Inset: Baseline fluorescence intensity of $(GT)_N$ suspensions at the (9,4) chirality (red) and change in fluorescence intensity after addition of 100 μM of dopamine (orange). (b) $(GT)_6$-SWNT nanosensor response curve for norepinephrine (red) and dopamine (black). Error bars are standard deviation from n = 3 independent measurements. Experimental data fit with Hill equation.

Conversely, 'long' $(GT)_N$ polymers (N = 12, 15, 19, 22, 26, 30), yield lower $\Delta F/F_0$ = 0.45, 0.4, 0.5, 0.6,0.4, and 1.5 responses to 100 μM DA, respectively (**Figure 4a**). They identify low baseline fluorescence, F_o, for 'short' $(GT)_{4\text{-}8}$-SWNT complexes as the reason for the large $\Delta F/F_0$ values of these constructs (**Figure 4a, inset**). The $(GT)_6$-SWNT construct shows increased selectivity towards a new neuromodulator target, NE, with $\Delta F/F_0$ = 35 sensitivity (**Figure 4b**). Concentration-dependent fluorescence response curves for $(GT)_6$-SWNT show fluorescence modulation for DA and NE lie within an optimal dynamic range for *in vivo* imaging of neuromodulation (100 nM to 2 μM) (**Figure 4b**).

2.3.2 DNA polymer length drives helix-to-ring transition on SWNT

To disclose the mechanisms that enable selective molecular recognition by ssDNA-wrapped SWNT optical nanosensors, we performed all-atom molecular dynamics (MD) simulations of these nanosensors. Variations in the optical signal (the PL quantum yield resulting

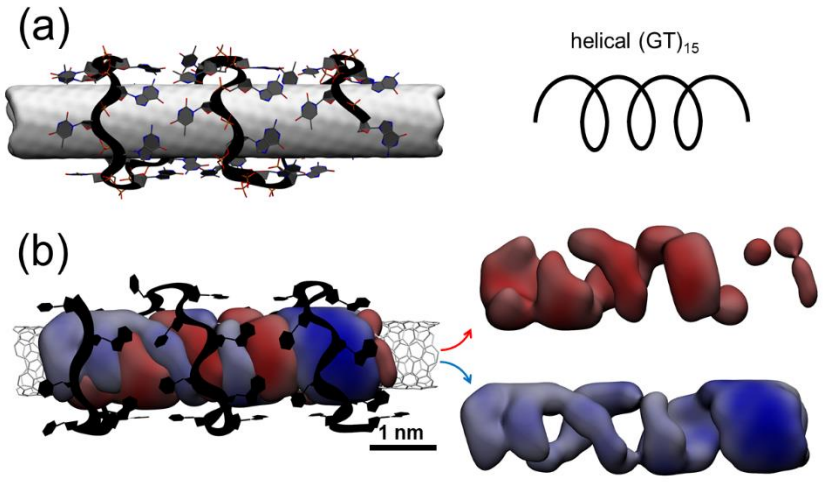

Figure 5 Helical conformation of $(GT)_{15}$ on SWNT. (a) A representative conformation of $(GT)_{15}$ wrapping SWNT. SWNT is shown as a white surface, $(GT)_{15}$ DNA and its backbone are shown in licorice and black ribbon representations. ssDNA atoms are shown in gray (C), red(O), blue(N) and orange(P). (b) The extended electrostatic potential pattern at the SWNT surface, beneath the adsorbed $(GT)_{15}$. Red and blue regions represent negative and positive potential domains, respectively. For clarity, the potential domains are shown separately on the right.

from exciton relaxation) of SWNTs wrapped by different polymers are known to depend on the chemical parameters of polymers, including their chemistry, and interaction types and strengths, and physical parameters of the SWNT environment, such as the dielectric screening [32]. Here we characterize the environment of the ssDNA-wrapped SWNTs, and examine how this environment affects their optical output.

In the present study, structures of several ssDNA-SWNT composites were examined, including ssDNA polymers containing a varying number of repeating (GT) units. The initial states of ssDNA-SWNT systems were based on previous observations [33-37], which determined that $(GT)_n$ polymers wrap SWNTs helically. During 200 ns simulations, $(GT)_{15}$-DNA on SWNT showed no significant structural deviations from its initial helical conformation, as shown in **Figure 5a**.

To examine the effect of $(GT)_{15}$ environment on SWNT, the electrostatic potential at the SWNT was calculated and shown in **Figure 5b**. The calculated potential takes into account the presence of the whole SWNT environment: ssDNA, water, and ions, including the Na^+ cations adsorbed over long timescales within DNA pockets. The regions of negative and positive electrostatic potential beneath $(GT)_{15}$ are extended (spanning ~4 nm lengths) and roughly follow the helical pattern of the ssDNA.

Figure 6 shows the residence time of Na^+ cations hosted by $(GT)_{15}$ bases. To confirm this observation, snapshots of typical $(GT)_{15}$ guanine and thymine bases hosting ions are provided in **Figure 7**. Additionally, **Figure 7** shows the radial distribution function (RDF) of sodium ions around O4' atoms of guanine and thymine bases, further confirming these sodium ions' binding pockets. These snapshots revealed two types of ion pockets including base's ring, sugar ring and phosphate groups of ssDNAs wrapping. The O4' atom of the sugar ring was the most difficult

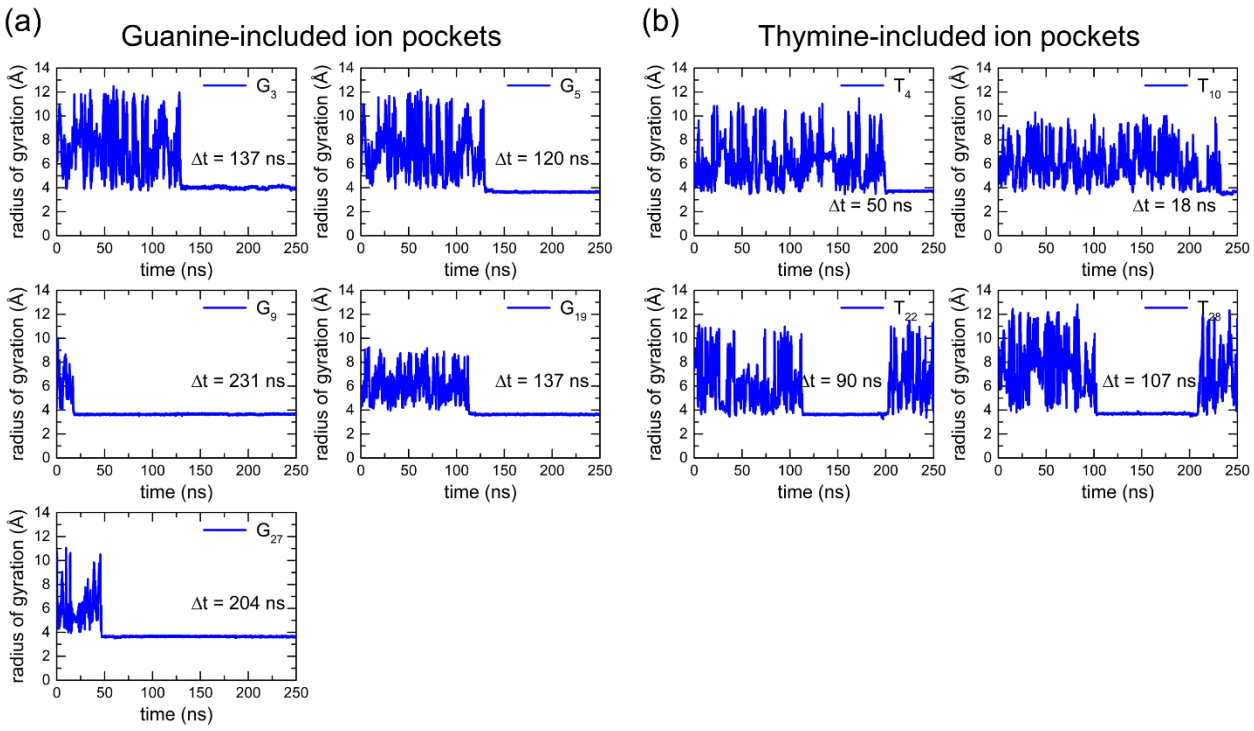

Figure 6 Residence times of Na^+ ions hosted by nucleotides of $(GT)_{15}$ DNA on (9,4) SWNT. (a) residence time of Na^+ ions by guanine. (b) residence time of Na^+ ions by thymine. The residence times were calculated based on radii of gyration of selected nucleotide atoms and trapped Na^+ ions.

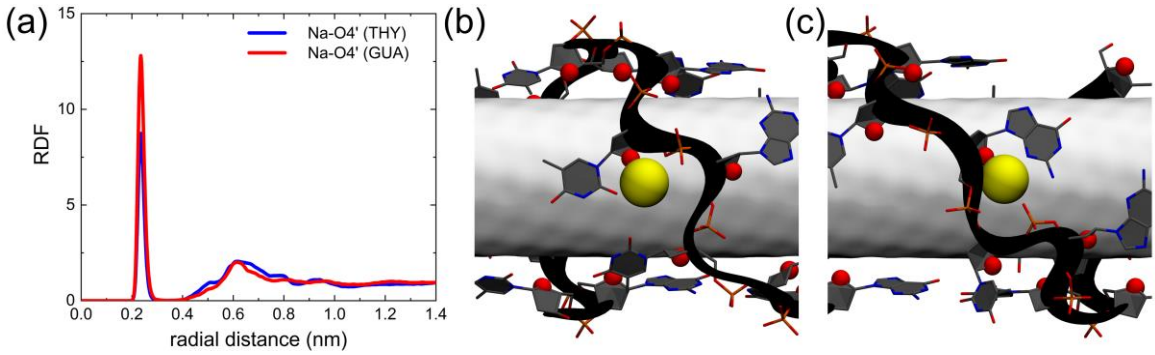

Figure 7 Ion hosting by $(GT)_{15}$ wrapping SWNT. (a) Sodium ions-O4' atoms RDF. (b) MD snapshots of thymine-involved ion pocket of $(GT)_{15}$. (c) MD snapshots of guanine-involved ion pocket of $(GT)_{15}$. Red and yellow balls represent O4' atoms and sodium ions, respectively. The other color schemes is the same as Figure 5.

atom to be reached by ions moving in the surrounding of ssDNA-wrapped SWNT except trapped and hosted ions premanently. To measure the density of cations, the RDFs of sodium ions and O4' of bases were calculated. Both guanine and thymine bases (turning toward O4' atom of sugar ring and two phosphate atoms) of $(GT)_{15}$ were capable of hosting sodium ions (**Figure 7a**).

While long DNA molecules that can wrap SWNTs several times are assumed to adopt helical conformations, shorter ssDNA oligonucleotides may adopt different SWNT surface adsorbed patterns [36], which can provide another control parameter over exciton relaxation mechanism. In particular, some of the SWNTs that are widely used for sensing have ~1.2 nm diameters, and they can accommodate a singly wrapped 12-mer (4.08 nm long) oligonucleotide, when rounding up to the nearest integer oligonucleotide. We modelled such oligonucleotide ($(GT)_6$) initially helically adsorbed to the surface of a (9,4) SWNT, to replicate the initial conditions of the simulated $(GT)_{15}$-SWNT system. During a short 20 ns simulation, $(GT)_6$ polymer rearranged from its initial helical conformation to a ring-like structure, displayed in **Figure 8a**; such helix-to-ring conversions were reproducibly observed in more than five independent MD simulations.

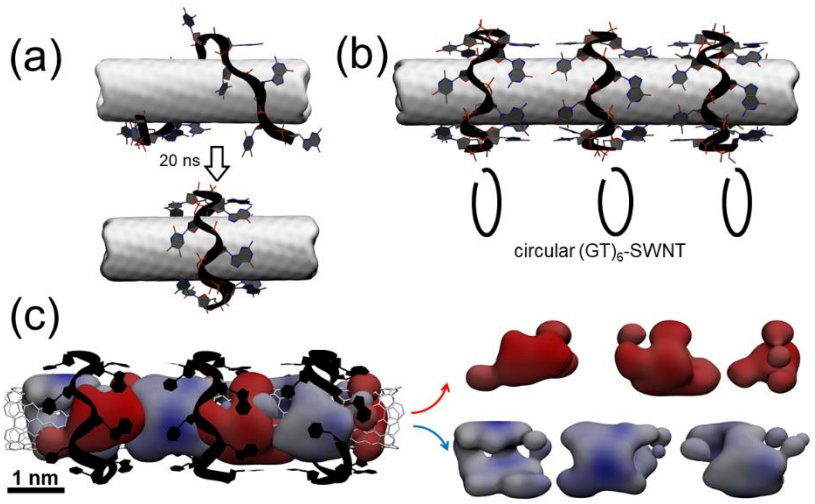

Figure 8 $(GT)_6$ forms ring-like structures at the SWNT. (a) $(GT)_6$ with initial helical conformation around SWNT (non-pre-adsorbed bases) switches to a ring-like conformation around the SWNT after 20 ns equilibration. (b) Multiple $(GT)_6$ polymers adsorbed to SWNT, resembling more realistic conditions in experiments. (c) The localized electrostatic potential patterns at the SWNT surface, beneath the adsorbed $(GT)_6$. Red and blue regions represent negative and positive potential domains, respectively. For clarity, the potential domains are shown separately on the right.

While the system shown in **Figure 8a** contains a single ssDNA molecule, the experimental systems contain many ssDNA molecules adsorbed onto SWNT. To better emulate experimental conditions, we next examined multiple $(GT)_6$ polymers wrapping the SWNT (**Figure 8b**). Following a 32 ns simulation, we again observe helix-to-ring transitions for $(GT)_6$ polymers. The DNAs in ring conformations are highly ordered, as evidenced by distinct sharp peaks that appear at approximately equal intervals in the RDF of DNA phosphate groups (**Figure 9a**). **Figure 9a** shows the comparison between the RDF of DNA phosphate groups of $(GT)_6$ with $(GT)_{15}$ wrapping the (9,4) SWNT. The same SWNT was used to simulate systems including either 3-$(GT)_6$ or a single $(GT)_{15}$. With this in mind, the ensemble averaged RDFs confirm that the structure of $(GT)_6$ wraps the SWNT much tighter and more ordered than $(GT)_{15}$. **Figure 9b** represents the ensemble averaged contact area between SWNT and either 3-$(GT)_6$ or $(GT)_{15}$ was computed to explain that the same SWNT accommodates more charged groups through adsorption of shorter sequences of ssDNA than longer ssDNAs, such as $(GT)_{15}$. It increases the polarity of environment of SWNT wrapped by shorter DNAs.

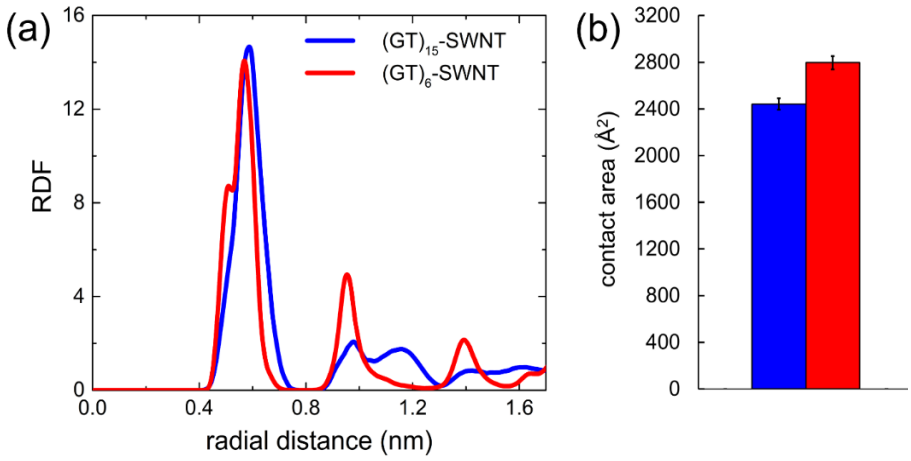

Figure 9 (a) Radial distribution functions of phosphate groups (P-atom) of $(GT)_{15}$ and $(GT)_6$ DNAs on SWNTs, calculated for the last 100 ns of simulations. (b) Contact areas between DNA molecules and SWNTs, averaged over the last 100 ns of simulations.

The electrostatic potential induced by the ring-like structures of $(GT)_6$ polymers is shown in **Figure 8c**. Again, the potential follows the $(GT)_6$ adsorption pattern on SWNT, resulting in distinct separated ring-like regions of alternating positive and negative potential along the SWNT surface, where each pocket measures ~1.5 nm on average. The negative potential is observed primarily beneath guanine nucleotides, while the positive potential is observed beneath the thymine nucleotides.

Hosted ions play a key role in influencing the polarity of SWNT environment. We also investigated the density and residence time of cations around the negatively wrapped SWNT by $3(GT)_6$. All $3(GT)_6$ wrapping SWNT hosted sodium ions. **Figure 10** represents the residence time of ions hosted by top, middle and down $(GT)_6$ molecules (along z-axis). In contrast to $(GT)_{15}$, The ions were mainly hosted by guanine bases of $(GT)_6$ DNAs. In addition, sodium ions are adsorbed to $(GT)_6$ DNAs much more permanently than $(GT)_{15}$ while wrapping SWNT. Adsorbed ions permanently hosted by $(GT)_6$ strengthens the polarity of environment of SWNT wrapped by $(GT)_6$ ssDNAs. The guanine bases of $(GT)_6$ hosted sodium ions for much longer than both guanine and

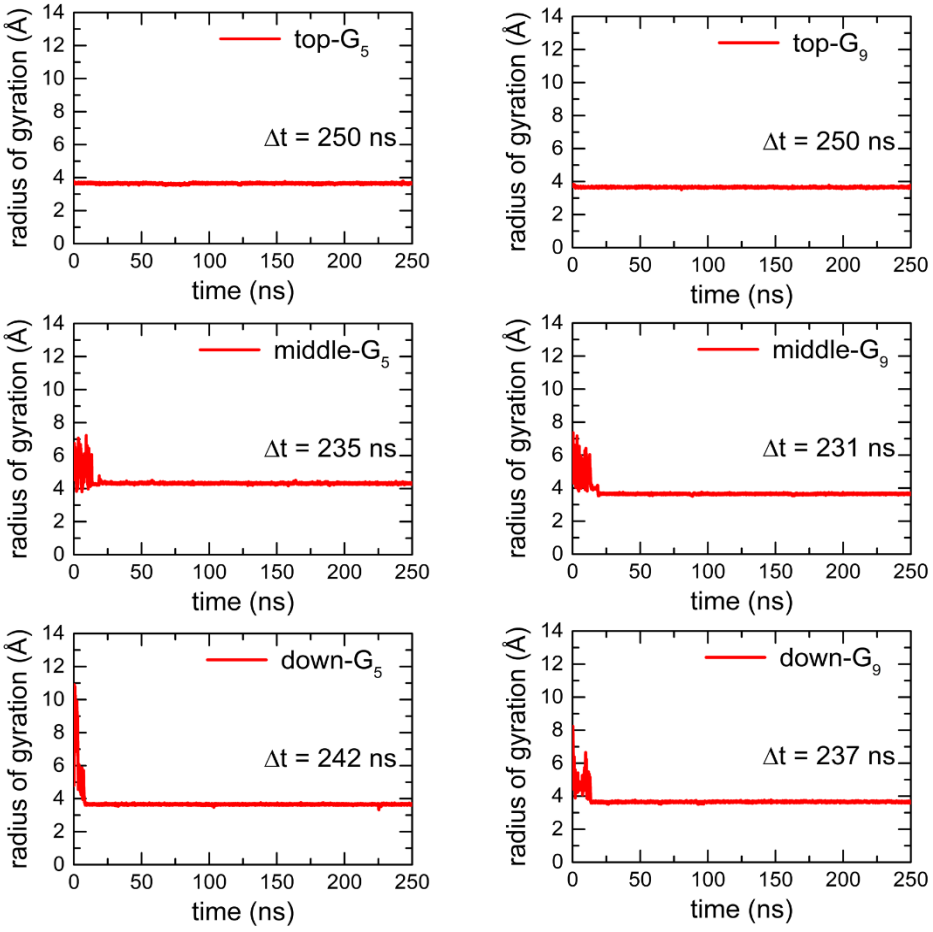

Figure 10 Residence times of Na^+ ions hosted by guanine nucleotides of $(GT)_6$ DNA on (9,4) SWNT. Guanine residues 5 and 9 of every single $(GT)_6$ molecule on SWNT hosted Na^+ ions (the analyzed system is shown in **Figure 8**, and top, middle and down refers to three $(GT)_6$ molecules). The residence times were calculated as in **Figure 6**.

thymine bases of $(GT)_{15}$. We found no thymine bases of $(GT)_6$ that hosted sodium ions permanently.

Simulation snapshots showing ion hosting by 3-$(GT)_6$ are presented in **Figure 11**. In the case of $(GT)_6$, only guanine bases were able to host and trap cations permanently (**Figure 11**). The RDF of sodium cations around O4' atoms of sugar ring confirms that the density of hosted sodium ions by $(GT)_6$ was higher than density of cations trapped by $(GT)_{15}$ wrapping SWNT.

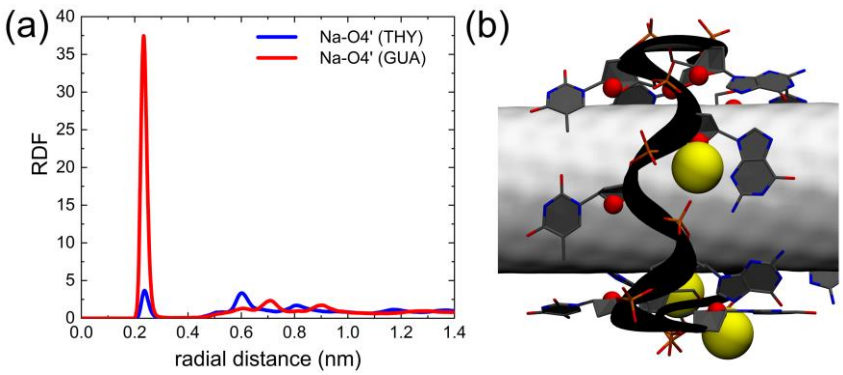

Figure 11 Ion hosting by ssDNAs wrapping SWNT. (a) Sodium ions-O4' atoms RDF. (b) MD snapshots of one ion pocket of $(GT)_6$. Red and yellow balls represent O4' atoms and sodium ions, respectively. The other color schemes is the same as Figure 5.

2.3.3 Adsorbed dopamine modulates ssDNA conformation and electrostatic potential at SWNT

To examine the molecular recognition mechanism of dopamine, we performed all-atom MD simulations of $(GT)_{15}$ and $(GT)_6$ -SWNT in the presence of dopamine. Several independent MD simulations revealed that dopamine can influence ssDNA conformations and that dopamine has multiple binding poses that are transient (binding lasts for ~ 20 – 214 nanoseconds).

Figure 12 shows representative binding poses of dopamine to $(GT)_{15}$. Dopamine binds to $(GT)_{15}$-SWNT so that it raises neighboring DNA bases (**Figure 12**). This binding pocket is located at the end of $(GT)_{15}$ and where two $(GT)_{15}$s probably meet. In addition, dopamine can create a binding pocket by inserting between two ending $(GT)_{15}$ pitches (one pitch is complete and another, the last one is incomplete). In this binding pocket, dopamine is trapped between the last pitch and two raised successive bases belonging to the pitch, which is before the last one.

In the case of $3(GT)_6$-SWNT, dopamine can insert into SWNT regions that transiently have no DNA coverage, and be stabilized by simultaneously stacking to the SWNT and hydrogen bonding to neighboring DNAs nucleotides. Occasionally, when dopamine stacks on SWNT, DNA nucleotides can also cover dopamine and form stacked sandwich-like structures (**Figure 12**).The bound dopamine contributes to the potential created at the SWNT surface. The bottom panels in **Figure 12 and 13** show the electrostatic potential beneath dopamine for several representative

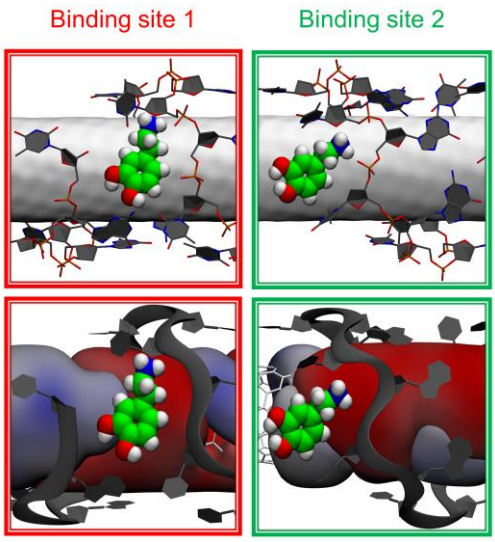

Figure 12 Adsorbed dopamine modulates ssDNA conformations and electrostatic potential at SWNT. Two representative binding poses of dopamine at $(GT)_{15}$-SWNT, and the corresponding electrostatic potential pattern at SWNT surface. Atoms of dopamine are shown in green (C), red (O), blue (N) and white (H). Color scheme for other molecules is the same as in **Figure 5**.

binding poses on the SWNT surface. Dopamine binding usually corresponds to extension of the potential regions. Such modulations in the potential are likely to affect exciton localization.

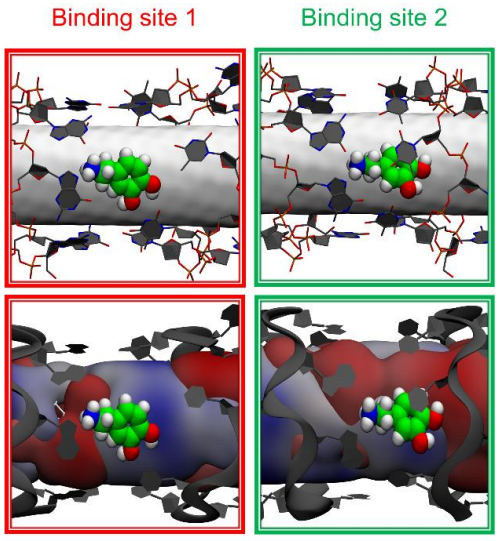

Figure 13 Adsorbed dopamine modulates ssDNA conformations and electrostatic potential at SWNT. Two representative binding poses of dopamine at $(GT)_6$-SWNT, and the corresponding electrostatic potential pattern at SWNT surface. The color scheme is the same as **Figure 5.**

2.3.3.1 *Residence time of trapped dopamine in binding sites*

Here, the residence time of dopamine trapped by $(GT)_{15}$-SWNT and $3(GT)_6$-SWNT structures are compared. **Figure 14** shows the residence time of dopamine trapped in binding sites, which were introduced in the previous section. The dopamine were permanently adsorbed to binding sites 1 and 2 of $(GT)_{15}$ wrapping SWNT (**Figure 14a**). In contrast to $(GT)_{15}$-SWNT system, dopamine is adsorbed to $(GT)_6$ wrapping SWNT intermittently (**Figure 14b**). This difference could be due to more dynamic and diffusive nature of $(GT)_6$ than $(GT)_{15}$ at SWNT. Additionally, dopamine trapped in $(GT)_{15}$ binding sites is much more involved in intermolecular interactions than dopamine trapped in $(GT)_6$ binding sites.

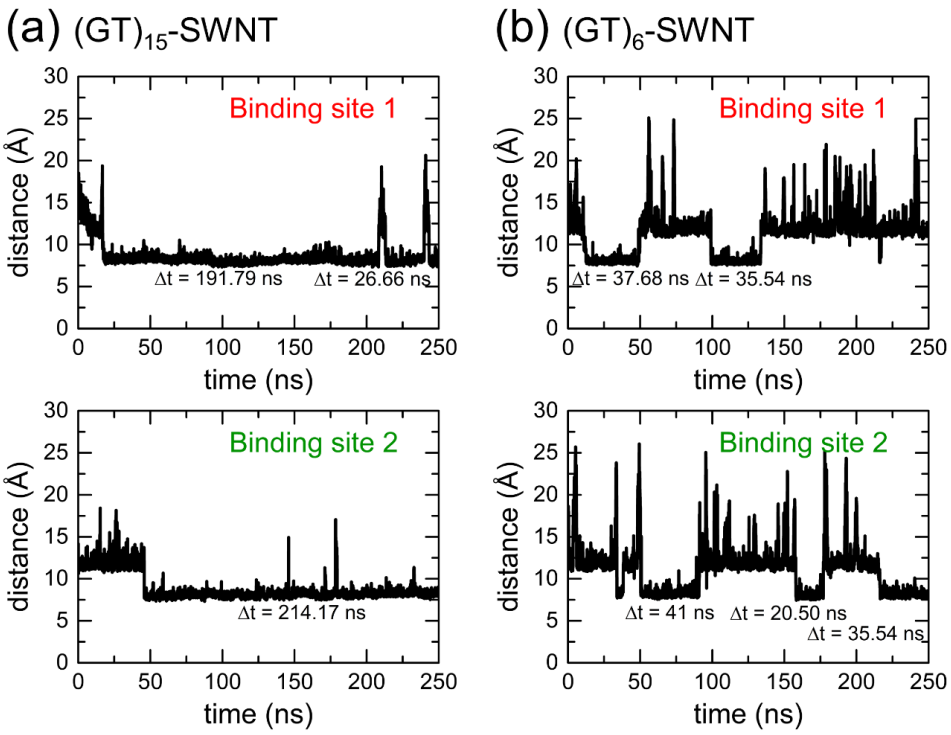

Figure 14 Residence times of dopamine molecules trapped in their binding sites. (a) Residence times of dopamine in $(GT)_{15}$-SWNT systems in binding sites 1 and 2. (b) Residence times of dopamine in $(GT)_6$-SWNT systems in binding sites 1 and 2. Residence times were calculated by tracking the radial distance between the dopamine ring center of mass and the central axis of SWNT. Dopamine binds more stably to $(GT)_{15}$ than to $(GT)_6$.

2.3.4 Excitonic interpretation of optical responses of circularly and helically ssDNA-wrapped SWNT

Experimental results showed that $(GT)_{15}$-SWNT and $(GT)_6$-SWNT hybrid materials have different optical response. Our simulation results also revealed that $(GT)_{15}$ and $(GT)_6$ polymers assume two distinct wrapping phases including helical and ring-like phases around SWNT. Accordingly, they created the above-discussed electrostatic potentials close to the SWNT surface. As mentioned above, negative potential pockets are primarily beneath guanine nucleotides, while positive pockets are beneath thymine nucleotides. When averaged over the radial SWNT dimension, as shown in **Figure 15a**, the electrostatic potential profile at SWNT surface under $(GT)_{15}$ is roughly constant (averaging across helix) with random fluctuations. In contrast to $(GT)_6$, however, when averaged over the radial SWNT dimension (**Figure 15b**), this electrostatic potential exhibits large periodic oscillations (averaging across rings). Given the fact that electrons, holes, and excitons confined in SWNTs have a quasi-1D nature, the periodic electrostatic potential created by the $(GT)_6$ rings (**Figure 15b)** effectively forms a superlattice.

To first check if the electrostatic potential in Figure 14b is a significant perturbation on the exciton, we calculated the binding energy between the electron and hole, described as Gaussian described in section 2.2.2. We found that the binding energy of electron and hole at a separation

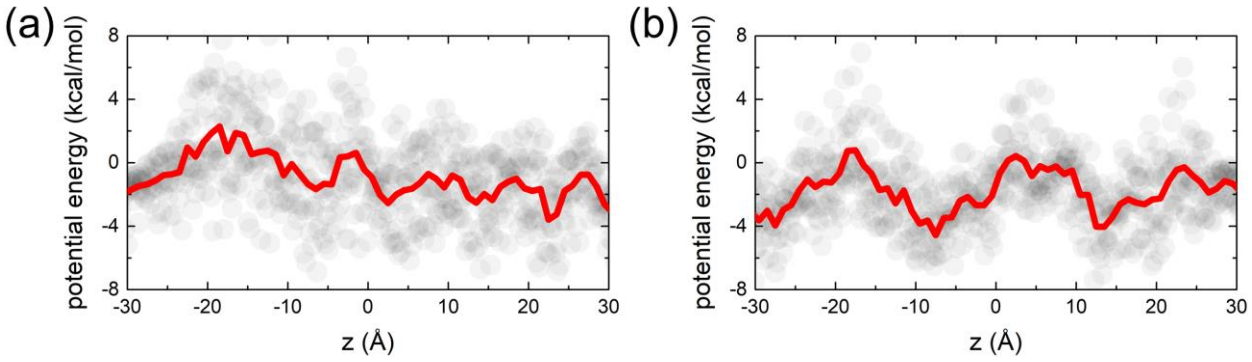

Figure 15 Electrostatic potential energy profiles at SWNT along z-axis. (a) Electrostatic potential energy profile at SWNT surface in $(GT)_{15}$-SWNT system as a function of SWNT length. The profile is averaged over 2 ns and over the radial SWNT dimension, and includes the effects of the complete SWNT environment present in MD simulations (ssDNA, water and ions). (b) Electrostatic potential energy profile at SWNT surface for $(GT)_6$-SWNT system, evaluated as in panel (a).

of ~2 nm is roughly 40 kcal/mol, which could be perturbed by the circumference averaged potential (red line, Figure 14b), whose amplitudes span the range of ~6 kcal/mol, or by the overall potential (grey dots, Figure 14b), whose amplitudes span the range of ~16 kcal/mol.

We believe that dopamine (as a positively charged species) adsorption on the DNA-wrapped SWNT decreases the SWNT polarization. But this effect is only **local**, meaning that low molarity of adsorbed and detected dopamines can't significantly depolarize a large $(GT)_6$-SWNT complex. The dopamine adsorption is also reflected in the appearance of perturbations in the periodic electrostatic potential, which can affect the luminescence.

The above results can be used to reveal possible relaxation pathways of excitons in the $(GT)_n$-SWNT complexes with/without loosely adsorbed dopamine. We can assume that: (1) Due to SWNT-polarization induced by the presence of multiple $(GT)_6$, a non-radiative exciton relaxation mechanism can occur in SWNT, since the effective doping activates phonon-assisted relaxation channels for excitons [38]. As discussed above, the adsorption of loose dopamines (1 molecule/3 $(GT)_6$ DNAs) can only slightly reduce the SWNT polarization, but it can't block this non-radiative exciton relaxation mechanism. (2) The radiative exciton relaxation can be largely

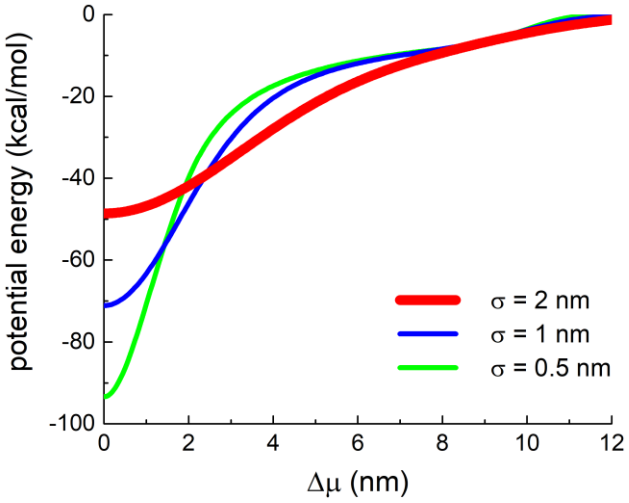

Figure 16 Electron-hole potential interaction energy. Potential energy of electron and hole particles (represented as Gaussian distributions) coupling in a cylindrical SWNT, evaluated in a dielectric environment with ε=4. The parameters σ and Δμ represent the spread and the center-to-center distance between the delocalized particles.

blocked by the presence of a periodic potential of multiple $(GT)_6$, shown in **Figure 15b**. In positive/negative regions of this potential, the electron and hole wave function components tend to avoid each other (**Figure 16**), which is accompanied by a significant cancelation of their overlap integral, present in the oscillator strength [39]. Therefore, in a pure $(GT)_{n=6}$-(9,4) SWNT complex (complete SWNT coverage) radiative transitions of excitons are expected to be significantly suppressed, in agreement with the experiments. However, in the presence of loosely adsorbed dopamine this blocking (cancellation of overlap integral) can be disturbed (disordered superlattice) and the radiative transitions can be active simultaneously with the non-radiative transitions [38], which matches the experimental observations. It also can be confirmed by comparing the adsorption of sodium ions, which are point charge species to dopamine binding sites at (9,4) SWNT wrapped by $(GT)_6$. Dopamine and sodium ions are positively charged species, however, their adsorption has different influence on optical properties of SWNT. It means, $(GT)_6$-(9,4) SWNT is dark in the presence of positively small ions, however only dopamine can disturb the superlattice structure and lead to radiative electron-hole recombination.

2.4 Conclusions

An ultrasensitive nanosensor composed of (9,4) SWNT wrapped by $(GT)_6$ to sense neurotransmitter molecules was suggested. In contrast to helical structure of longer ssDNAs, such as $(GT)_{15}$ around SWNT, $(GT)_6$ assumes a ring-like structure wrapping (9,4) SWNT. We proposed several binding sites of dopamine at (9,4) SWNT wrapped by either $(GT)_{15}$ or $(GT)_6$. The residence time of dopamine on binding sites at $(GT)_{15}$-SWNT is much more permanent than residence time of dopamine at $(GT)_6$-SWNT. In comparison to helical wrapping phase of $(GT)_{15}$ wrapping SWNT, the periodic charged rings at SWNT are capable of leaving oscillatory electrostatic potential forming a quantum well, which leads to cancellation of overlap integral of electron and hole wave functions. In fact, these periodic, stable and charged rings at SWNT mimic superlattice structure and cancel electron-hole wave function overlap. However, adsorption of dopamine

disturb the superlattice structure and cause radiative electron-hole recombination explaining the ultra-sensitivity of $(GT)_6$-(9,4) SWNT.

3 Free Energy Landscape of Ring-like DNA-SWNT

3.1 Introduction

The rapid and efficient detection of molecular analytes stands to be transformative for numerous fields of science and technology. Since many important molecular analytes lack molecular recognition elements, the development of selective sensors for such analytes is limited. One class of such important molecular analytes are modulatory neurotransmitter molecules. There is a critical need for development of neurotransmitter sensors that will eventually be capable to probe the emergence, diagnosis, and treatment of neurological disease by providing quantitative measures of the neurochemical environment in cells and tissues.

An important example of neurotransmitter sensors includes SWNTs functionalized with specific DNA sequences, which were found to be responsive to several neurotransmitter molecules. In our preliminary studies done with Prof. Markita Landry (UC Berkeley) and Michael Strano (MIT), and jointly published in PNAS [40] and J. Phys. Chem. C [41], we observed that DNA-wrapped SWNTs were successful in imaging neurotransmitters in proof-of-concept experiments in *in vitro* and cellular environments. Our results showed that variations in polynucleotide sequence can lead to large changes in the conformational stability of the nucleic acid at the SWNT surface and the SWNT optical response.

Recently, Landry group determined that (9,4) SWNTs wrapped by a short oligonucleotide sequence, $(GT)_6$, exhibit remarkably quenched baseline fluorescence that vigorously recovers in response to neuromodulators norepinephrine and dopamine. Our detailed modeling of (GT)N-SWNT systems was described above in Chapter 2. The turn-on response of DNA-wrapped (9,4) SWNTs was found to be a function of the sequence length. Our preliminary MD simulations show that $(GT)_6$ polymers adopt ordered, ring-like conformations around SWNT, in contrast to the helical conformations observed for longer DNA sequences (Chapter 2 above).

3.2 Methods

3.2.1 Free energy calculations

To confirm the suggested novel ssDNA structure on the SWNT surface, we performed free energy calculations to make the short ssDNA-SWNT systems explore the phase space and enhance our sampling. The free energy landscape was obtained through replica exchange MD (REMD) simulation of a $(GT)_6$-SWNT system solvated in $3.63 \times 3.63 \times 4.92$ nm^3 box, containing 6,605 atoms. The box contained 1,881 water molecules, modeled using TIP3P model. In addition to Na^+ counterions neutralizing the system, 36 Na^+ and Cl^- ions were included to meet the physiological salt concentration in the system. Periodic boundary conditions were imposed in all dimensions, and PME method was used to calculate long-range electrostatics. Additionally, both ends of SWNT are in contact with their periodic images. Energy minimization and 100 ps of heating (NVT) were performed to reach the starting temperature of 310 K. To perform REMD simulation in NVT ensemble, 54 replicas and 290-727.4 K temperature range were chosen to maintain exchange acceptance ratios around 25% with 2 ps exchange time. The total REMD simulation time was 54×270 ns (per replica) = 14.58 μs. The simulation time step was 2 fs and trajectories were extracted every 2 ps. Therefore, 135,000 configurations per replica were collected. The last 80,000 (160 ns) configurations of room temperature replica were analyzed to obtain the free energy landscape.

To generate the free energy landscape, two independent order parameters of $(GT)_6$ structure were calculated from the obtained system configurations: 1) end-to-end distance of DNA molecule (the z-distance between centers of mass of the first guanine and last thymine residues; z coordinate aligns with the long axis of the SWNT); and 2) RMSD of phosphorous atoms of DNA backbone, compared to the configuration these atoms have in the ideal left-handed helix of $(GT)_6$ wrapping SWNT. The probability distribution function ($P(x, y)$) of these two order parameters were calculated and combined to generate free energy ($\Delta F(x, y)$) according to the formula:

$$\frac{\Delta F(x,y)}{k_B T} = -\ln\left(\frac{P(x,y)}{P_{max}}\right)$$

In above formula, P_{max} is the maximum value of $P(x,y)$. The free energy landscape was obtained at temperature of 300 K by calculating two-dimensional free energy landscape according to above formula, where x and y represent end-to-end distance and RMSD of left-helix ssDNA wrapping SWNT, respectively.

3.3 Results and Discussions

3.4 Ring conformation of DNA on SWNT

The optical response of DNA-wrapped SWNT sensors depends on DNA length (**Figure 4**) and sequence [40]. Therefore, we hypothesized that $(GT)_N$ polymers influence the SWNT optical response by assuming different conformations on the SWNT surface. To examine the above hypothesis, we studied $(GT)_6$-SWNT, $(GT)_7$-SWNT, and $(GT)_{15}$-SWNT hybrids in preliminary atomistic MD simulations. In all these simulations, DNA molecules initially wrapped SWNTs in helical conformations, as reported in Refs. [33-37]. $(GT)_{15}$ and $(GT)_7$ remained in helical conformations on SWNTs during 200 ns trajectories. Unexpectedly, $(GT)_6$ polymer reproducibly

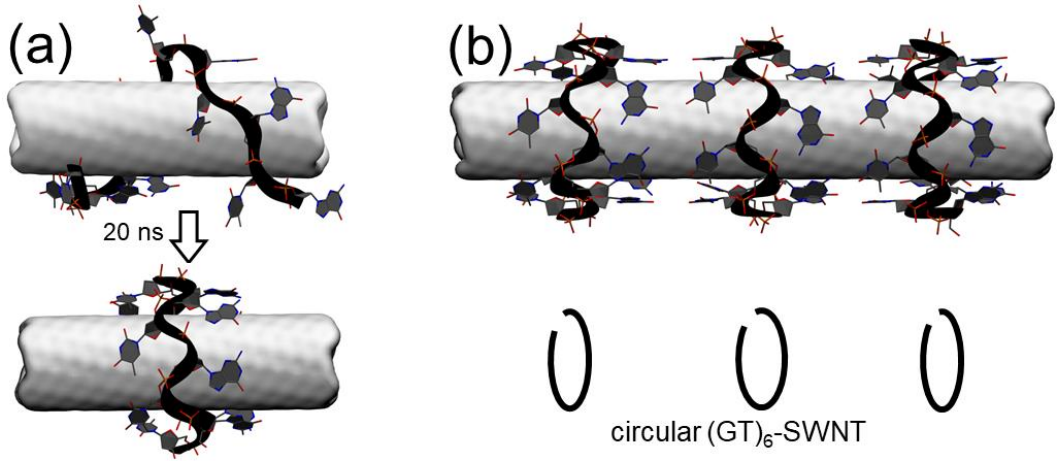

Figure 17 $(GT)_6$ assumes a ring-like conformation on (9,4) SWNT. (a) one $(Gt)_6$ forms ring-like structure around SWNT after 20 ns. (b) A representative conformation of $(GT)_6$-SWNT, containing three $(GT)_6$ molecules. SWNT is shown as a gray surface, $(GT)_6$ and its backbone are shown in licorice and black ribbon representations, and ssDNA atoms are shown in gray (C), red (O), blue (N) and orange (P).

rearranged from its initial helical conformation to a ring-like conformation in five independent MD simulations, as discussed in Chapter 2 and as shown in **Figure 17a**. Multiple $(GT)_6$ molecules also reproducibly assumed ring-like conformations (**Figure 17b**).

3.4.1 Free energy landscape of ring DNA at SWNT surface

To confirm that the ring-like conformation of $(GT)_6$ is truly a favorable state, the free energy landscape of $(GT)_6$ molecule on SWNT surface should be determined. REMD is one of the reliable methods to determine the free energy landscape of $(GT)_6$ molecule on SWNT. This method was used previously by R. Johnson, et al. to determine the free energy landscape of $(GT)_7$ conformations at the (6,5) SWNT surface [36], where several minimum free energy conformations of $(GT)_7$ were found, including the helical and C-shaped conformations along the SWNT length.

To examine the free energy landscape $(GT)_6$ molecule on (9,4) SWNT, we prepared *a minimal system* that we could simulate with REMD method on the limited resources available to us. The free energy landscape of the minimal system, shown in **Figure 18**, reveals two distinct stable conformations of $(GT)_6$, a left-handed helix and a ring-like conformation, corresponding to

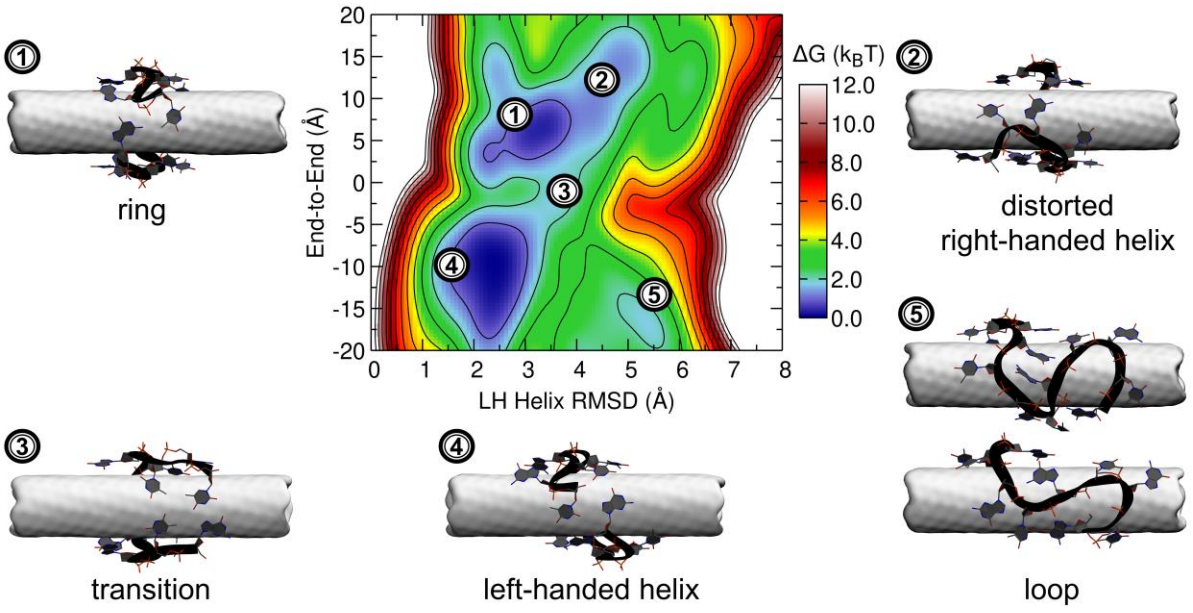

Figure 18 Free energy landscape of $(GT)_6$-SWNT at 300 K. The structures corresponding to two free energy minima are labeled by indices 1 and 4.

the free energy minima at (2.5 Å, -8 Å) and (3 Å, 5 Å), respectively. Free energies of these two conformations differ by ~ k_BT, and thus should be the dominant conformations of $(GT)_6$ on SWNT at room temperature. The free energy barrier between the two conformations, ~2 kcal/mol, suggests that frequent conversion between the conformations should be observed at room temperature. The stability of helical and ring conformations can be explained by increase in entropy of ssDNA conformation and water, respectively. A proper analogy may be drawn between protein folding pathway and formation of ring at SWNT surface where the entropy of structures decrease, however the entropy of water as the solvent drives the folding pathway forward.

In a realistic case, (9,4) SWNT dispersed by $(GT)_6$ could be covered by many rings. In fact, the packing density of $(GT)_6$ at the SWNT surface increases if $(GT)_6$ assumes ring structure around (9,4) SWNT. This was confirmed by experiments where increasing the concentration of dispersant $(GT)_6$ results in stronger fluorescence quenching. These experiments suggest that (9,4) SWNT is covered by more rings if there are more $(GT)_6$ molecules trying to cover and be adsorbed at the (9,4) SWNT by changing the helical $(GT)_6$ at SWNT to ring $(GT)_6$ while wrapping SWNT.

Our calculations also successfully reproduced the other suggested structures of ssDNA at SWNT in a previous study [36]. Distorted "right-handed helix" and loop structures (panel 2 and 5 of **Figure 18,** respectively) at (9,4) SWNT were observed as two other structures having free energy minima.

3.5 Conclusions

Through using REMD simulation, two most stable structures of $(GT)_6$ including ring-like and helical structures wrapping (9,4) SWNT were obtained. The energy barrier between two structures is small enough to expect that the helical structure changes to ring structure and vice versa in the course of simulation at room temperature. In experiments, realistic (9,4) SWNT dispersed by $(GT)_6$ is covered by many rings as non-adsorbed $(GT)_6$ molecules try to cover the surface by forcing helical $(GT)_6$ to form a ring around SWNT circumference. Therefore, the ring-like structure of $(GT)_6$ wrapping (9,4) SWNT could be much more stable structure while non-

adsorbed $(GT)_6$ molecules try to cover circumference of SWNT by changing helical to ring-like conformation of $(GT)_6$.

References

1. G. Hong, S. Diao, A. L. Antaris, H. Dai, Carbon nanomaterials for biological imaging and nanomedicinal therapy. *Chemical reviews* **115**, 10816-10906, (2015).
2. Z. Liu, S. Tabakman, K. Welsher, H. Dai, Carbon nanotubes in biology and medicine: in vitro and in vivo detection, imaging and drug delivery. *Nano research* **2**, 85-120, (2009).
3. Y. Liu, X. Dong, P. Chen, Biological and chemical sensors based on graphene materials. *Chemical Society Reviews* **41**, 2283-2307, (2012).
4. S. F. Oliveira, G. Bisker, N. A. Bakh, S. L. Gibbs, M. P. Landry, M. S. Strano, Protein functionalized carbon nanomaterials for biomedical applications. *Carbon* **95,** 767-779, (2015).
5. S. Kruss, M. P. Landry, E. Vander Ende, B. M. Lima, N. F. Reuel, J. Zhang, J. Nelson, B. Mu, A. Hilmer, M. S. Strano, Neurotransmitter detection using corona phase molecular recognition on fluorescent single-walled carbon nanotube sensors. *Journal of American Chemical society* **136**, 713-724, (2014).
6. E. S. Snow, F. K. Perkins, E. J. Houser, S. C. Badescu, T. L. Reinecke, Chemical detection with a single-walled carbon nanotube capacitor. *Science* **307**, 1942-1945, (2005).
7. R. H. Baughman, A. A. Zakhidov, W. A. De Heer. Carbon nanotubes--the route toward applications. *Science* **297**, 787-792, (2002).
8. G. Hong, S. Diao, J. Chang, A. L. Antaris, C. Chen, B. Zhang, S. Zhao et al, Through-skull fluorescence imaging of the brain in a new near-infrared window. *Nature photonics* **8**, 723-730, (2014).
9. J. Zhang, M. P. Landry, P. W. Barone, J. Kim, S. Lin, Z. W. Ulissi, D. Lin et al. Molecular recognition using corona phase complexes made of synthetic polymers adsorbed on carbon nanotubes. *Nature nanotechnology* **8**, 959-968, (2013).
10. J. Kim, D. A. Heller, H. Jin, P. W. Barone, C. Song, J. Zhang, L. J. Trudel, G. N. Wogan, S. R. Tannenbaum, M. S. Strano, The rational design of nitric oxide selectivity in single-walled carbon nanotube near-infrared fluorescence sensors for biological detection. *Nature Chemistry* **1**, 473-481, (2009).
11. G. Bisker, J. Dong, H. D. Park, N. M. Iverson, J. Ahn, J. T. Nelson, M. P. Landry, S. Kruss, M. S. Strano, Protein-targeted corona phase molecular recognition. *Nature communications* **7,** 10241, (2016).
12. N. M. Iverson, G. Bisker, E. Farias, V. Ivanov, J. Ahn, G. N. Wogan, M. S. Strano. Quantitative tissue spectroscopy of near infrared fluorescent nanosensor implants. *Journal of biomedical nanotechnology* **12**, 1035-1047, (2016).
13. C. Gurvich, S. L. Rossell, Cognition across the psychiatric disorder spectrum: From mental health to clinical diagnosis. *Frontiers in psychiatry* **6** (2015).
14. A. P. Alivisatos, A. M. Andrews, E. S. Boyden, M. Chun, G. M. Church, K. Deisseroth, J. P. Donoghue et al. Nanotools for neuroscience and brain activity mapping. *ACS nano*, **7**, 1850-1866, (2013).
15. J. C. Phillips, R. Braun, W. Wang, J. Gumbart, E. Tajkhorshid, E. Villa, C. Chipot, R. D. Skeel, L. Kale, K. Schulten, Scalable molecular dynamics with NAMD. *Journal of Computational Chemistry* **26**, 1781-1802 (2005).

16. J. Huang, A. D. MacKerell, CHARMM36 all-atom additive protein force field: Validation based on comparison to NMR data. *Journal of Computational Chemistry* **34**, 2135-2145 (2013).
17. S. E. Feller, A. D. MacKerell, An improved empirical potential energy function for molecular simulations of phospholipids. *The Journal of Physical Chemistry* B **104**, 7510–7515 (2000).
18. J. B. Klauda, R. M. Venable, J. A. Freites, J. W. OConnor, D. J. Tobias, C. MondragonRamirez, I. Vorobyov, A. D. MacKerell, R. W. Pastor, Update of the charmm all-atom additive force field for lipids: Validation on six lipid types. *The Journal of Physical Chemistry* B **114**, 7830–7843 (2010).
19. T. Darden, D. York, L. Pedersen, Particle mesh Ewald: An N·log(N) method for Ewald sums in large systems. *Journal of Chemical Physics* **98**, 10089 (1993).
20. G. Torrie, J. Valleau, Nonphysical sampling distributions in monte carlo free-energy estimation: Umbrella sampling. *Journal of Computational Physics* **23**, 187–199 (1977).
21. E. Darve, A. Pohorille, Calculating free energies using average force. *Journal of Chemical Physics* **115**, 9169–9183 (2001).
22. T. P. Straatsma, H. J. C. Berendsen, Free energy of ionic hydration: Analysis of a thermodynamic integration technique to evaluate free energy differences by molecular dynamics simulations. *Journal of Chemical Physics* **89**, 5876–5886 (1988).
23. J. Aaqvist, Ion-water interaction potentials derived from free energy perturbation simulations. *The Journal of Physical Chemistry* **94**, 8021–8024 (1990).
24. Y. Sugita, Y. Okamoto, Replica-exchange molecular dynamics method for protein folding. *Chemical Physics Letters* **314**, 141-151 (1999).
25. P. Král and B. Wang, Material Drag Phenomena in Nanotubes, Chem. Rev. **113**, 3372 (2013).
26. W. Humphrey, A. Dalke, K. Schulten, VMD - Visual Molecular Dynamics, *Journal of Molecular Graphics* **14**, 33-38 (1996).
27. Materials Studio (R); Accelrys Inc.: San Diego, CA, (2005).
28. K. Vanommeslaeghe, E. Hatcher, C. Acharya, S. Kundu, S. Zhong, J. Shim, E. Darian, O. Guvench, P. Lopes, I. Vorobyov, A. D. Mackerell, CHARMM general force field: A force field for drug-like molecules compatible with the CHARMM all-atom additive biological force fields. *Journal of Computational Chemistry* **31**, 671–690 (2010).
29. W. Yu, X. He, K. Vanommeslaeghe, A. D. MacKerell, Extension of the charmm general force field to sulfonyl-containing compounds and its utility in biomolecular simulations. *Journal of Computational Chemistry* **33**, 2451–2468 (2012).
30. I. N. Levine, D. H. Busch, H. Shull, Quantum chemistry. Vol. 5. *Upper Saddle River, NJ: Prentice Hall* (2000).
31. D. A. Heller, R. M. Mayrhofer, S. Baik, Y. V. Grinkova, M. L. Usrey, M. S. Strano, Concomitant length and diameter separation of single-walled carbon nanotubes. *Journal of the American Chemical Society* **126**, 14567-14573 (2004).
32. T. Hertel, H. Sabine, A. Thomas, S. Dominik, C. Jared, Diffusion limited photoluminescence quantum yields in 1-D semiconductors: single-wall carbon nanotubes. *ACS nano* **4**, 7161-7168 (2010).
33. B. Gigliotti, B. Sakizzie, D. S. Bethune, R. M. Shelby, J. N. Cha, Sequence independent helical wrapping of single-walled carbon nanotubes by long genomic DNA. *Nano Letters* **6**, 159-164 (2006).

34. R. R. Johnson, AT. C. Johnson, M. L. Klein, Probing the structure of DNA− carbon nanotube hybrids with molecular dynamics. *Nano Letters* **8**, 69-75 (2008).
35. G. Dukovic, M. Balaz, P. Doak, N. D. Berova, M. Zheng, R. S. Mclean, L. E. Brus, Racemic single-walled carbon nanotubes exhibit circular dichroism when wrapped with DNA. Journal of the American Chemical Society **128**, 9004-9005 (2006).
36. R. R. Johnson, A. Kohlmeyer, A. C. Johnson, M. L. Klein, Free energy landscape of a DNA−carbon nanotube hybrid using replica exchange molecular dynamics. *Nano Letters* **9**, 537-541 (2009).
37. S. Manohar, T. Tang, A. Jagota, Structure of Homopolymer DNA−CNT Hybrids. *The Journal of Physical Chemistry C* **111**, 17835–17845 (2007).
38. V. Perebeinos, P. Avouris, Phonon and Electronic Nonradiative Decay Mechanisms of Excitons in Carbon Nanotubes. *Physical Review* Letters **101**, 057401 (2008).
39. E. L. Ivchenko, V. P. Kochereshko, P. S. Kop'ev, V. A. Kosobukin, I. N. Uraltsev, D. R. Yakovlev, Exciton Longitudinal-Transverse Splitting in GaAs/AlGaAs Superlattices and Multiple Quantum Wells. *Solid State Communications* **70**, 529-534 (1989).
40. S. Kruss, D. P. Salem, L. Vuković, B. Lima, E. Vander Ende, E. S. Boyden, M. S. Strano, High-resolution imaging of cellular dopamine efflux using a fluorescent nanosensor array. *Proceedings of the National Academy of Sciences* **114**, 1789-1794 (2017).
41. M. P. Landry, L. Vukovic, S. Kruss, G. Bisker, A. M. Landry, S. Islam, R. Jain, K. Schulten, M. S. Strano, Comparative dynamics and sequence dependence of DNA and RNA binding to single walled carbon nanotubes. *The Journal of Physical Chemistry C* **119**, 10048-10058 (2015).

Vita

Aliasghar (Ali A.) Alizadehmojarad was born in a town, Esfarayen located in the Northeast of Iran in 1989. He finished high school studies (as a 1st ranked student) in the same town, he then got accepted by The University of Tehran which is the oldest and most prestigious university in Iran. He earned his B.Sc. (2011) and M.Sc. (2014) degrees in Chemical Engineering while he was on the Dean's List for both studies.

He enjoys studying complex systems by applying molecular simulation methods, which will find much broader applications one day. He published two articles in peer-reviewed journals based on his M.Sc. thesis in Iran. He also attended 253rd ACS meeting in San Francisco, USA and gave two talks about his research under supervision of Prof. Lela Vuković. He is a member of American Chemical Society and Iran Society of Engineering Education.

Contact Information: ali.alizadehmoj@gmail.com